J. Fluid Mech. (1981), *vol.* 102, *pp.* 1–59
Printed in Great Britain

Array measurements of atmospheric pressure fluctuations above surface gravity waves

By R. L. SNYDER,
Nova University
F. W. DOBSON, J. A. ELLIOTT
Bedford Institute of Oceanography
AND R. B. LONG
Atlantic Oceanographic and Meteorological Laboratories

(Received 7 February 1979 and in revised form 1 February 1980)

A joint experiment to study microscale fluctuations of atmospheric pressure above surface gravity waves was conducted in the Bight of Abaco, Bahamas, during November and December 1974. Field hardware included a three-dimensional array of six wave sensors and seven air-pressure sensors, one of which was mounted on a wave follower. The primary objectives of the study were to resolve differences in previous field measurements by Dobson (1971), Elliott (1972*b*) and Snyder (1974), and to estimate the vertical profile of wave-induced pressure and the corresponding input of energy and momentum to the wave field.

Analysis of a pre-experiment intercalibration of instruments and of 30 h of field data partially removes the discrepancy between the previous measurements of the wave-induced component of the pressure and gives a consistent picture of the profile of this pressure over a limited range of dimensionless height and wind speed. Over this range the pressure decays approximately exponentially without change of phase; the decay is slightly less steep than predicted by potential theory. The corresponding momentum transfer is positive for wind speeds exceeding the phase speed. Extrapolation of present results to higher frequencies suggests that the total transfer is a significant fraction of the wind stress (0·1 to 1·0, depending on dimensionless fetch).

Analysis of the turbulent component of the atmospheric pressure shows that the 'intrinsic' downwind coherence scale is typically an order-of-magnitude greater than the crosswind scale, consistent with a 'frozen' turbulence hypothesis. These and earlier data of Priestley (1965) and Elliott (1972*c*) suggest a horizontally isotropic 'intrinsic' turbulent pressure spectrum which decays as $k^{-\nu}$ where k is the (horizontal) wave-number and ν is typically -2 to -3; estimates of this spectrum are computed for the present data. The implications of these findings for Phillips' (1957) theory of wave growth are examined.

1. Introduction

The statistical evolution of the surface wave field in deep water is governed by a radiative transfer equation of the form (Hasselmann 1960),

$$\frac{\partial}{\partial t}E_{\zeta^2}+\mathbf{V}.\nabla E_{\zeta^2}=A_{\zeta^2}+N_{\zeta^2}+D_{\zeta^2}, \tag{1}$$

0022-1120/81/4577-2590 $02.00

where $E_{\zeta^2}(\omega, \theta)$ is the spectral density of surface elevation (directional spectrum) at horizontal position $\mathbf{x}$ and time t for the wave component with radial frequency ω and propagation direction θ, $\mathbf{V}(\omega, \theta)$ is the group velocity of this component, and ∇ is the horizontal gradient operator (note that bold face denotes a two-dimensional horizontal vector). The terms on the left-hand side of (1) govern the propagation of the spectral density field. The terms on the right-hand side represent dynamical sources (or sinks) of spectral density: A_{ζ^2} is the atmospheric source function, N_{ζ^2} is the nonlinear transfer term and D_{ζ^2} represents dissipative effects such as whitecapping and bottom friction. The understanding of these source terms is the ultimate objective of much current research on ocean waves.

Of the three terms, N_{ζ^2} is at present best known, having been derived theoretically by Hasselmann (1962); D_{ζ^2} is least well known both theoretically and experimentally (a recent theory by Hasselmann, 1974, suggests that this term is proportional to $\omega^2 E_{\zeta^2}$); A_{ζ^2} has been the subject of intense interest for many years, starting with the pioneering theoretical work of Phillips (1957) and Miles (1957), who identified two of its components. Both components of A_{ζ^2} involve a transfer of energy and momentum from wind to waves by the working of air pressure fluctuations on the moving water surface, in the one case resonant turbulent fluctuations (Phillips), and in the other case fluctuations induced by the sheared mean wind blowing over the wavy surface (Miles). The former produce a linear change of spectral density with time, the latter an exponential change.

Previous experimental efforts to study the evolution of the wave field include some which have monitored the left-hand side of (1) (e.g. Snyder & Cox 1966; Barnett & Wilkerson 1967; Hasselmann *et al.* 1973), and others which have estimated the Miles component of the atmospheric input by monitoring wave-induced air-pressure fluctuations above the water surface (e.g. Longuet-Higgins, Cartwright & Smith 1963; Shemdin & Hsu 1967; Dobson 1971; Elliott 1972*b*; Snyder 1974). This latter task has proved difficult. Besides the usual instrumentation problems associated with accurate measurement of static pressure fluctuations in the presence of a fluctuating velocity field, additional problems result from the motion of the water surface. If the air-pressure probe is fixed (Elliott 1972*b*; Snyder 1974), it can be no closer to the mean surface than the highest wave crest. In order to compute the energy and momentum transfer to the wave field, the resulting measurements must be extrapolated to the mean surface, requiring some knowledge of the vertical structure of the air-pressure field. If the instrumentation follows the surface (Longuet-Higgins *et al.* 1963; Shemdin & Hsu 1967; Dobson 1971), other problems arise, including contamination of the pressure signal by inertial and hydrostatic effects, by spray and splashing, etc. Moreover, in order to deal with the directional properties of both the surface elevation and the air pressure fields, measurements should be made simultaneously at a number of horizontal positions, an operation requiring an array of wave sensors and air-pressure sensors.

The earlier independent measurements of wave-induced air pressure by Dobson, Elliott and Snyder emphasized single aspects of the experimental task while ignoring or dealing only partially with other aspects. Dobson avoided a vertical extrapolation by mounting a single air-pressure sensor in a buoy constrained to slide up and down on a vertical staff, but made no attempt to resolve the directional characteristics of the wave and wave-induced air-pressure fields (he assumed these fields to be unidirec-

tional). His analysis, which is complicated by buoy motions and by the effects of splashing, produces large phase shifts (relative to potential theory) and an integral momentum transfer comparable with the wind stress. Moreover, this analysis implies a wave growth comparable to that observed by Snyder & Cox, suggesting that on the low-frequency face of the spectrum in the region of active generation, A_{ζ^2} is the important source term.

This conclusion was placed in doubt by Elliott, who employed a two-component vertical array of fixed air-pressure sensors in order to extrapolate his observations to the mean surface. Elliott's analysis (which also assumes that the wave and wave-induced air-pressure fields are unidirectional) suggests that away from the mean surface the wave-induced air-pressure field decays essentially exponentially without change of phase, but this decay is somewhat less rapid than is predicted by potential theory. Elliott's phase shifts are moderate and his implied growth rates are only a fraction (roughly $\frac{1}{5}$) of those implied by Dobson.

Still smaller phase shifts and growth rates resulted from Snyder's measurements. Using a horizontal array of fixed air-pressure sensors and wave sensors in order to deal more realistically with the directional characteristics of the wave and air-pressure fields, Snyder extrapolated his observations to the mean surface on the basis of potential theory. A subsequent analysis supports this extrapolation but is unable to distinguish between it and other 'near' potential theory extrapolations such as Elliott's.

Two cooperative attempts to overcome the inadequacies of the earlier experiments were included in the September 1973 JONSWAP effort in the North Sea. The first of these, utilizing Elliott's fixed vertical array and a newly constructed wave-follower-mounted pressure sensor (Harvey & Dobson 1976) managed, despite hostile environmental conditions, to acquire some limited data (Dobson & Elliott 1978). The second attempt, utilizing a four-component horizontal array of wave sensor/air-pressure sensor pairs simultaneously positioned at different elevations (Snyder & Long) and a wave-follower-mounted pressure sensor (Shemdin), failed to produce any data because the instrumentation could not be deployed.

Following JONSWAP 1973, the authors decided to undertake still another cooperative experiment to measure air-pressure fluctuations, in this case at Nova University's Bight of Abaco experimental site. The primary objectives of the experiment were to resolve as far as possible the differences in previous results, and to make a new experimental determination of A_{ζ^2} in which both the vertical structure of the air-pressure field and the directionality of the wave and air-pressure fields would be treated simultaneously. The experiment began with a careful laboratory intercalibration of instruments and comparison of calibration techniques (§2). This intercalibration was followed by the field experiment (§3). The resulting data were analysed at the Bedford Institute of Oceanography using essentially the same techniques previously applied by Dobson and Elliott (§§4, 5 and 6). At Nova a model-fitting scheme was used which incorporates mean current, wave-induced air-pressure vertical structure, wave and air-pressure field directionality, and a model of the turbulent pressure field (§§4, 5, 7 and 8). The implications of these analyses are examined in §9, and final conclusions summarized in §10.

Instrument	Transducer	No.	Units	Range	Accuracy	Resolution†	Noise† (0·1–1 Hz)	Drift (60 min)	Frequency† (Hz)
Air-pressure sensors									
Elliott sensor	Datametrics 'Barocel' 11–10 differential pressure transducer	2	Pa	13·3	0·01	0·001	0·01	0·5	0·01–10
Nova sensor	Decker 360G differential pressure transducer	4	Pa	25	—	0·01	0·05	—	0·01–1
Wave-follower sensor	Kaman Nuclear K-1000-1 differential pressure transducer	1	Pa	20	0·3	0·05	—	5·0	0·01–10
Wave sensors									
BIO wave staff	N.S. Research Foundation resistance-wire gauge	1	m	6·7	0·01	0·002	0·01	0·01	0–3
Nova water-pressure sensor	Viatran 218–15 strain gauge differential pressure transducer	4	Pa	3×10^4	100	10	20	5	0–1
Wave-follower piston-position sensor	Computer Instruments 13130–1 Potentiometer	1	m	0·92	0·002	0·002	0·001	0·001	0–2
Wave-follower tracking-error sensor	R. Flower capacitance gauge	1	m	0·38	0·01	0·001	0·004	0·01	0–10
Environmental sensors									
Nova tide gauge	D. Hunley reed switch gauge	1	m	1·5	0·01	0·01	—	—	0–0·001
Cup anemometer	Thornthwaite	3	m s^{-1}	—	0·2‡	—	—	—	0–0·01
Wind vane	Taylor	1	deg	350	5	1	—	—	0–0·01
Sonic anemometer	Kaijo-Denki PAT-III	1	m s^{-1}	60	—	—	—	—	0–10
EMCM	Cushing 612-K	1	m s^{-1}	1	0·03	0·0005	0·001	—	0–0·01
BCCM	Pabst BR	1	m s^{-1}	—	—	—	—	—	—
TPCM	Northern 2-ply	1	m s^{-1}	—	—	—	—	—	—

† Figures for Nova instruments are system figures.
‡ At 10 m s^{-1}.

TABLE 1. Instrument list.

2. Instrumentation and intercalibration

The instruments used in the experiment are listed in table 1. They fall into three categories: air pressure sensors (including two types of fixed sensors and a wave-follower-mounted sensor), wave sensors, and environmental sensors (such as wind speed, wind direction, tide level and current).

The sensing head for the first type of fixed air-pressure sensor (Elliott 1972*a*) is a shaped thin brass disk, 4 cm in diameter, mounted with its plane horizontal. The pressure is sensed at two ports on opposite sides of the disk and is fed downwind through a tapered 'sting' to a differential pressure transducer inside a waterproof housing. The pressure sensed through the disk is compared with the pressure in a 'reference-volume' Dewar flask inside the housing. System response is fixed at low frequency by a leak (time constant 15 s) from the reference volume to the atmosphere, and at high frequency by constrictions in the instrument's plumbing. The sensing disk has a pressure coefficient of $< 0{\cdot}01$ over a range of pitch angles of $\pm 10°$.

The second type of fixed air-pressure sensor (Snyder *et al.* 1974) was specifically designed for and has been previously used for atmospheric pressure fluctuation measurements at the Bight of Abaco site (Snyder 1974). The pressure is sensed by a cone-shaped probe connected via a 3 m standpipe to a subsurface differential pressure transducer. The transducer is housed with sump, backing volume, and capillary leak in a foam-insulated canister, mounted on a stand. The probe has a pressure coefficient of $< 0{\cdot}02$ magnitude for angles of attack in the range $\pm 15°$; a wind vane minimizes horizontal angles of attack.

The wave follower air-pressure transducer is mounted at the top of the wave-follower piston. The plane of its diaphragm is almost vertical and is aligned with the 'downwind' direction of the sensor package, which can itself be oriented into the wind. An accelerometer is used to correct the pressure signal for accelerations perpendicular to the plane of the diaphragm. The pressure is sensed by an Elliott disk and is fed to the transducer via a low-friction rotating seal. It is mounted vertically and kept within $\pm 10°$ of the instantaneous wind direction by a small vane. The transducer is sealed inside a small Dewar flask, which insulates it and also provides a reference volume. The flask is vented to the atmosphere via a 15 s time constant leak.

Because the wave follower has a finite frequency response, the pressure disk is located slightly down-wave from the wave sensing wire, introducing a spatial lag which approximates the temporal lag of the wave follower. This allows the pressure sensor to remain at approximately the correct tracking height.

The wave follower, described in detail by Harvey & Dobson (1976), is a direct descendant of a similar instrument developed at Chesapeake Bay Institute by Peep & Flower (1969). A 'sensor package' carrying the pressure sensor, thin-wire capacitance wave gauge and accelerometer is maintained at 'constant' level relative to the instantaneous water surface by an electro-hydraulic servo mechanism which controls the velocity of a supporting piston to minimize the difference (or 'error') between a fixed voltage and the signal from the capacitance wave gauge. The follower produces four signals: piston height $h(t)$ (measured with a precision potentiometer), tracking error $e(t)$, air pressure $K(t)$, and horizontal acceleration $H(t)$. The surface elevation $\zeta(t)$ (at the capacitance gauge) is computed from

$$\zeta(t) = h(t) + e(t).$$

A second wave sensor, the BIO wave staff, is constructed from a length of Nichrome wire wound helically with a 0·4 cm pitch on a flexible hollow nylon form 6·7 m long. The nylon form is clamped between two brackets to a length of wire rope running vertically inside the form. Additional water-pressure wave sensors employing strain-gauge pressure transducers were mounted directly on the subsurface canisters associated with the Nova air-pressure sensors. Base-line drift of these instruments was sufficiently low that the signal mean could serve as an acceptable measure of the vertical position of the air pressure and water pressure probes relative to the mean surface.

Mean water level was monitored with a reed switch tide gauge with a step size of 1·2 cm designed and built by D. Hunley (unpublished). The wind profile was determined by a vertical array of three cup anemometers. Wind direction was measured with a wind vane. Wind velocity and wind stress were also measured directly with a sonic anemometer (Mitsuta 1968).

Several techniques were used to sporadically monitor the mean water current. Owing to electronic problems a two-component electromagnetic current meter gave no results. For some runs a simple drogue, fashioned from a can and a small styrofoam float, was timed over a measured distance, giving the average current speed and direction at a depth of 1·5 m. On other runs, a piece of tissue paper was dropped and timed over a known distance as it sank from the surface to a depth of about 0.5 m. In fact, the 'effective' mean currents employed in the later data analyses were computed (see §7) as part of the directional spectrum analysis.

The intercalibration phase of the experiment was conducted at Nova University's Ocean Sciences Center during the several weeks prior to the field experiment. Objectives were:

(1) to compare laboratory calibration techniques for the air-pressure sensors;

(2) to establish final calibrations for all field instruments; and

(3) to estimate the reliability of the instrument calibrations.

Of particular interest was the evaluation of a suspected difficulty with earlier calibrations of the Nova air-pressure sensors.

Both groups had previously built pressure generators to aid in the calibration of their air-pressure instruments (Elliott 1972*a*; Snyder *et al.* 1974). To determine the response of a given instrument, the output of either generator is piped simultaneously to the instrument and to a 'standard' pressure transducer. By driving the generator at various frequencies and comparing the amplitudes and phases of the outputs of the instrument and of the standard, one can estimate the response of the instrument. An independent estimate of this response can be computed for the Nova generator from its physical dimensions and from the relative phase of its piston. This computation assumes an isothermal change of pressure.

The analysis of previous field experiments in the Bight of Abaco (Snyder 1974) had been based on a series of calibrations using a 'Decker' transducer as a standard, accepting the manufacturer's static calibration, and assuming instantaneous response over the frequency range of interest. A moderate roll off in the output of this transducer above 0·6 Hz, when driven directly by the Nova pressure generator, had been attributed to a failure of the generator to produce full theoretical output rather than to a lack of response by the transducer.

As a test of this assumption, the Nova pressure generator was calibrated directly

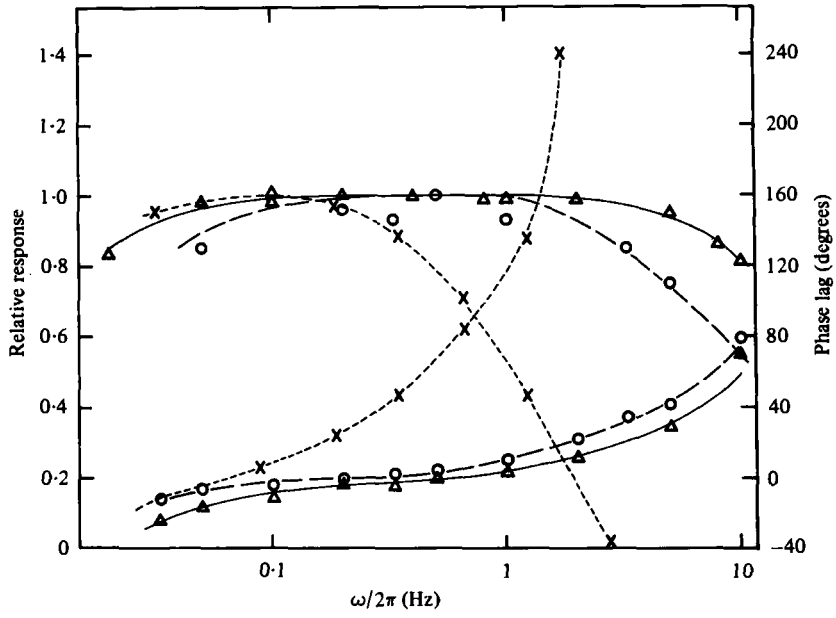

FIGURE 1. Response of air pressure sensors: ×, Nova sensor; ○, Elliott sensor; △, wave-follower sensor.

against one of the BIO 'Barocel' transducers. Below 1 Hz the amplitudes and phases of the Barocel agreed with the theoretical output of the Nova pressure generator to within 3% and 2°, respectively. Above 1 Hz, a roll off in the output of the Nova pressure generator was evident.

These results are consistent with the following conclusions.

(1) The Barocel transducer has instantaneous response to 1 Hz and beyond (prior tests at BIO suggest that this response is instantaneous to 10 Hz).

(2) The output of the Nova pressure generator is well predicted by theory at frequencies below 1 Hz.

(3) Below 1 Hz, the reliability of a careful calibration with either pressure generator is approximately 3% in amplitude and 2° in phase.

(4) The Decker transducer does not have instantaneous response to 1 Hz.

(5) Previous results for the Bight of Abaco are biased accordingly.

The possibility of such a bias was recognized by Snyder *et al.* (1974), who estimated the corresponding error in instrument response. The principal effect of this error is to decrease the observed air-pressure phase shift (relative to potential theory) and hence to decrease the corresponding estimates of energy and momentum transfer. A recomputation of figure 14 from Snyder (1974) is presented in figure 9. Comparison with the original figure reveals minor differences for $1 < \mu < 2$ with noticeable differences in both Im γ and Arg γ for $2 < \mu < 3$, where μ and γ are dimensionless wind-speed and growth-rate parameters (§6). Except for the location of the phase minimum, the new figure is in rough agreement with Elliott (1972*b*). This correction increases Snyder's momentum transfer by about a factor of 2; in all other respects the conclusions of his study are essentially unchanged.

Following the comparison of intercalibration techniques, final response calibrations were established for all air pressure sensors; typical responses are shown in figure 1.

Note the wider bandwidth of the BIO instruments (designed to study high-frequency turbulent pressure fluctuations as well as wave-induced fluctuations) as compared with the Nova instruments (designed primarily to study the central portion of the wave-induced spectrum).

The considerable historical data associated with past calibration of both the Elliott sensor and the Nova sensor suggest that the calibration of both instruments is relatively stable. Overall reliability is essentially the same as the reliability of an individual calibration, i.e. 3% in amplitude and 2° in phase. The wave follower pressure sensor, on the other hand, showed some short-term drift in gain (about $\pm 5\%$) during the intercalibration period; this drift was traced to a temperature sensitivity in the pressure transducer. Space and weight limitations on the wave-follower sensor package and time constraints forbade any attempt to eliminate the effect; it was decided instead to rely on frequent field 'calibration' runs with all sensors held at the same fixed height, and to accept a generally lower accuracy standard for the wave-follower pressure sensor (see table 1).

Because of its motion, the wave follower pressure sensor is subject to several errors not present with fixed sensors. During the intercalibration period the correction procedures for these special 'inertial' errors were checked. Accelerations of the pressure transducer diaphragm are monitored by an accelerometer, calibrated within $\pm 10\%$ by moving the sensor package in a cross-wind direction and recording its output together with that of the pressure sensor (in the field, this acceleration correction is typically very small). The sensitivity of the air column between the sensing head and the diaphragm to vertical acceleration was dealt with by tilting the pressure-transducer diaphragm 12° from vertical, allowing a small fraction of the acceleration sensitivity of the diaphragm to cancel out the effect of the air column. Prior to the permanent fixing of the transducer tilt (in July 1973) the vertical acceleration sensitivity was checked and found to vanish. The tilt of the sensor was also checked before the present experiment, but the acceleration sensitivity was not. A subsequent calibration, done at BIO under ideal conditions in June 1977, revealed that the sensor (still tilted at $12 \pm 1°$) was now sensitive to vertical accelerations, and was producing an acceleration-dependent signal

$$K(t) = -r \frac{d^2}{dt^2} h(t) \tag{2}$$

with $r \simeq 0{\cdot}25\,\mathrm{Pa\,s^2\,m^{-1}}$. Subsequent analysis suggests that the instrument was responding to vertical accelerations throughout the experiment (see §4).

The wave-follower surface elevation signal is recovered by summing the piston height and tracking error signals. A static calibration of piston height was performed and was stable to $\pm 1\%$ and linear to $\pm 1\%$ of full scale. The static sensitivity of the tracking-error probe (the probe has no measurable salinity dependence above 10‰) was found stable to $\pm 5\%$, and the mean offset (which determines the tracking level) to $\pm 15\%$. It was therefore decided to perform frequent field calibrations. The frequency response of the tracking error probe has subsequently been determined optically at 2–3·5 Hz. Extrapolation indicates that at lower frequencies this response is not significantly different from 1·0 in amplitude and $0 \pm 5°$ in phase. Note that the response of the error probe is included in the overall response of the wave-follower servo system and is thus accounted for in the analysis (§4).

The BIO wave staff was calibrated statically prior to the experiment by lowering it and raising it in measured increments in the water dockside at Nova's Ocean Sciences Center. A later field comparison between the wave staff and a Nova water-pressure sensor indicates that the response of both sensors is identical (and presumably instantaneous) below 1 Hz. Although the wave staff is linear to $\pm 0{\cdot}1$ cm of water level, the gain is somewhat temperature sensitive, leading to an overall accuracy of $\pm 2\,\%$. When checked against independent measurements of mean water level during the field experiments, the wave staff was found to be within $\pm 0{\cdot}05$ m.

Static calibrations of the Nova water pressure sensors were obtained using a water manometer. Base-line drift was monitored over a period of several weeks and found to be within the transducer manufacturer's specifications. Subsequent experience with the sensors suggests that in the field the drift was somewhat larger, resulting in a vertical position uncertainty of 0·02 to 0·04 m for the Nova instruments (air-pressure and water-pressure sensors).

The sonic anemometer was calibrated prior to and following the experiment in the wind tunnel at BIO and electronically in the field. In general, the calibrated sensitivities in the instrument's different ranges were within $\pm 1\,\%$ of the measured wind speed.

Additional response calibrations, related to the acquisition of BIO data on Nova's data-acquisition system (discriminators and anti-aliasing filters) concluded the intercalibration phase of the experiment.

3. Field experiment

The site chosen for the field experiment is in the Bight of Abaco (BOA), Bahamas, at a point approximately 5 km south of Black Point, Little Abaco (figure 2). This was also the principal site employed by Snyder (1974); a permanent instrument tower had been erected to support environmental instrumentation during this and previous experiments. Water depth in the area averages 7·6 m and is modulated by a tidal cycle of about 0·5 m peak-to-peak. The bottom is smooth and essentially flat, and consists of a thin layer of silt overlying bedrock.

The primary instrument array (figure 2, inset) was laid out 100 m northwest of the site tower during a preliminary cruise in the summer of 1974, when five steel tripod instrument bases were installed (figure 3). Each tripod was ballasted with a railroad wheel, and additional wheels were laid down as anchors for guy wires to support the BIO instrumentation mast. The orientation of the array and its position relative to the tower were chosen to take advantage of the strong northeast–east winds which accompany cold frontal passages commonly experienced in this region in winter.

During the experiment, each tripod supported a remotely controlled device to adjust the vertical position of the instrument mounted on it. The BIO wave follower was erected on the central tripod; a 12 m section of aluminium radio mast, set up along the southwest side of this tripod, supported the BIO fixed air-pressure sensors, the sonic anemometer, and the resistance-wire wave staff. The position of the fixed sensors could be adjusted both horizontally and vertically, and it was possible to place the probes directly above the wave follower air-pressure sensor. Nova instrument packages were mounted on the remaining four tripods, each package comprising an air-pressure sensor and a water-pressure wave sensor. The air-pressure probes

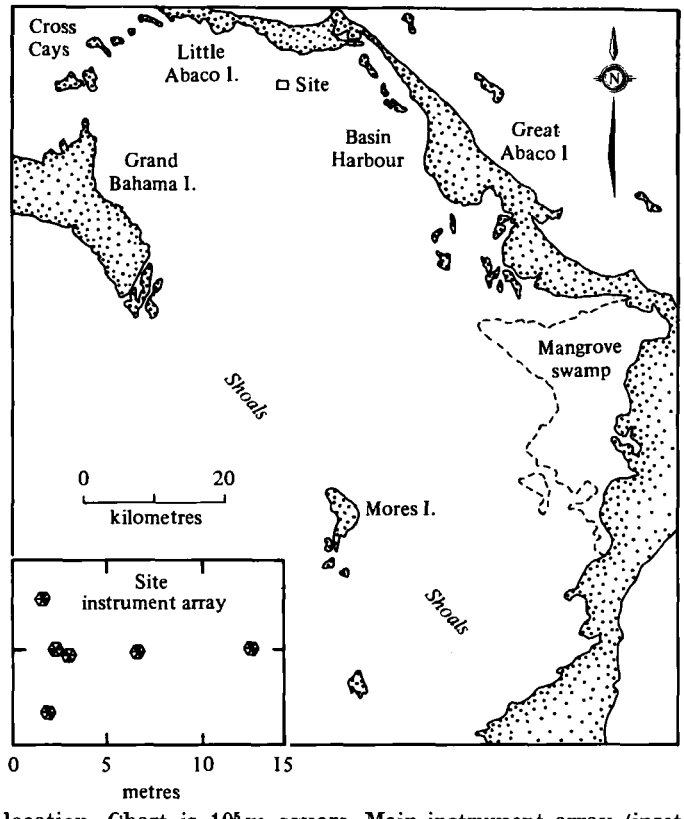

FIGURE 2. Site location. Chart is 10^5 m square. Main instrument array (inset): configuration for wave follower run 30. Scale is 5 m per division. ⊛, Elliott air-pressure sensor (2); ⊛, Nova air-pressure sensor; ⊛, wave-follower pressure sensor; ⊛, wave staff; ⊛, Nova water-pressure sensor; ⊛, wave-follower tracking sensor.

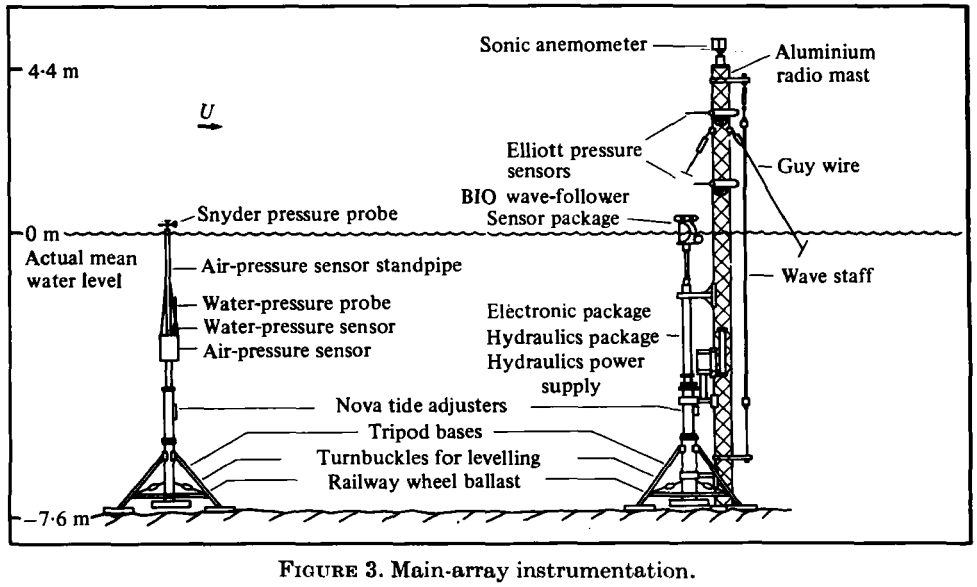

FIGURE 3. Main-array instrumentation.

could be positioned at elevations up to 2 m above the mean water surface. As the corresponding water-pressure sensor moved up and down with the air-pressure probe, its average reading provided a measure of the elevation of the air-pressure probe relative to the mean surface.

The site tower supported a tide gauge, a wind vane, and an array of three cup anemometers mounted in a vertical stack 1·5 m southeast of the tower. The anemometers were at heights of 1·31 m, 2·89 m, and 4·48 m above mean water level.

All instruments were connected by cables running across the bottom to the research vessel *Calanus*, moored approximately 100 m southeast of the tower (200 m southeast of the main instrument array). The field data were acquired aboard the *Calanus* using two acquisition systems, BIO's 12-channel FM telemetry system, and Nova's digital data-acquisition system, recently expanded to 32 high-speed channels and 8 low-speed channels. Use of a dual-recording system provided redundancy, and allowed each group later to pursue separately various aspects of the data analysis in terms familiar to them. Only the BIO signals were acquired on the FM system. Signals from all high-speed instruments listed in table 1, excepting the sonic anemometer, were acquired on the Nova system. To limit aliasing, a number of these signals were multiply sampled. The wave-follower error and wave-follower pressure signals also were passed through anti-aliasing filters prior to acquisition. In addition to the high-speed signals, the following low-speed signals were acquired on the digital system: wind speed (3 channels), wind azimuth, mean surface elevation, and mean current (2 channels). Base sample rate for the high-speed channels was 3·2 samples per second (total rate, 96 samples per second); sample rate for the low-speed channels was 0·75 sample per minute.

The field experiment began on November 24 with the arrival of the University of Miami's laboratory vessel, *Calanus*, and Snyder's ketch, *Catspaw*, in the Bight. A base camp was established at Basin Harbor Cay, a small island east of the site, where the participants' families stayed during the experiment, providing moral and logistic support. The supporting structures, cabling, and most of the instrumentation were installed at the site during the period 25–30 November, after which work was interrupted for three days by a strong frontal passage (winds west–northwest at 10 to 15 m s^{-1}). Following the front, the remaining instrumentation was installed.

The collection of data began on 6 December and continued on an intermittent basis until 18 December; a summary of the data runs is presented in table 2. These runs divide into groups according to instrument mix, meteorology, and the presence or absence of real or electronic contamination of the signals. In runs 5, 7, 11, 17 and 32 there was evidence of pressure port blockage or misalignment due to rain or sea water or vibration for one or more of the probes. In run 2, the WF pressure signal was contaminated by low-frequency fluctuations in sunlight intensity; in subsequent runs a sunshade was used. Runs 13, 23, 24, 28, 30, and 35 were taken during somewhat stationary wind or wave conditions. Runs 3, 4, 27, 33, and 34 were WF tracking runs, and runs 1, 6, 26, 29, 36, and 37 were 'calibration' runs with the WF pressure sensor in operation but at a fixed level.

During runs 10, 14, 31, 32, 33, and 36 the wave field was felt to be contaminated by upwind-travelling waves. In several of these (10, 14, and 32) this contamination was intended, with a reflector (Snyder's 11 m ketch *Catspaw*) or a wave generator (a 5 m 'Boston Whaler' (run 32)) placed downwind of the array; in runs 31 and 33 some cross-

Run	Type[1]	Day[2]	Time[2]	Length (min)	Wind Speed[3] (m s^{-1})	Wind Azimuth[4] (°)	Friction velocity[3] (m s^{-1})	Stability[5]	Current Speed[6] (m s^{-1})	Current Azimuth[4,6] (°)	Wave height[7] (m)	Wave Period[8] (s)	Wave Azimuth[4] (°)	Remarks
1	*B*	06	1629	29·3	3·41/3·38	061	0·116/0·124	0·017	0·10/0·13	055/141	0·177	2·0	111	
2	*B*	07	1509	45·2	4·17/4·24	084	0·131/0·181	0·027		120/	0·221	2·2		9
3	*A*	07	1659	42·6	2·59/2·71	090	0·076/	0·143	/0·17	/062	0·238	2·2	123	Tracking height 0·09 m
4	*A*	10	1020	47·5	4·66/	350	0·173/	−0·129	0·12/	340/	0·247	1·9		Tracking height 0·10 m. 10
5	*A*	10	1141	42·5	4·95/	348	0·212/	−0·072	0·13/0·18	335/246	0·243	1·9	328	Tracking height 0·05 m. 9
6	*B*	10	1444	39·8	5·37/	357	0·210/	−0·140			0·281	1·9		10
7	*A*	10	1745	43·8	4·21/	005	0·173/	−0·175			0·161	1·5		Tracking height 0·05 m. 9
8	*C*	11	1830	43·8	/2·32	069			/0·27	/087	0·068	2·2	065	11
9	*C*	12	1651	47·8	/2·94	107					0·084	2·2		
10	*C*	12	1752	27·9	1·88/1·77	087	0·043/	0·190	/0·13	/042	0·072	2·1	133	*Catspaw* downwind of array
11	*D*	13	0849	41·2	/4·82	111	/0·294				0·158	2·0		13
12	*F*	13	1146	45·2	5·93/4·86	133	0·172/0·208	0·078			0·273	2·3		
13	*D*	13	1048	42·5	6·49/	358	0·220/0·178	0·030	/0·13	/357	0·304	1·6	013	Sea rising during run
14	*C*	14	1208	43·8	5·96/5·85	039	0·172/0·220		/0·15	/109	0·248	2·1	061	*Catspaw* downwind of array
15	*C*	14	1315	42·5	6·51/6·51	039	0·221/0·220		/0·14	/020	0·280	2·3	069	
16	*C*	14	1424	43·8	6·02/5·86	050	0·168/0·238	0·068	0·07/0·13	049/001	0·306	2·5	069	
17	*C*	14	1521	42·5	6·66/6·51	048	0·210/0·241	0·048	/0·14	/002	0·320	2·4	069	
18	*C*	14	1651	43·8	6·19/6·17	050	0·208/0·249	0·039	/0·15	/355	0·363	2·6	073	13
19	*C*	14	1835	43·8	6·22/5·95	054	0·191/0·239	0·027	/0·15	/001	0·316	2·5	074	
20	*C*	14	1943	37·2	7·02/6·73	061	0·224/0·233	0·004	/0·05	/062	0·420	2·7	076	BIO recorded only first 13·5 min
21	*E*	15	0204	40·0	4·47/	080	0·128/	0·017			0·300			
22	*C*	15	0306	42·5	4·44/4·46	086	0·136/0·197	0·039	/0·06	/326	0·285	2·5	118	
23	*C*	15	0406	41·2	3·57/3·74	103	0·267/0·174	−0·042	/0·15	/204	0·278	2·4	107	12, 16
24	*C*	15	0517	42·5	3·83/3·60	094	0·106/0·195	−0·029	/0·07	/214	0·211	2·4	131	15
25	*C*	15	0627	41·2	5·06/4·94	095	0·169/0·203	−0·008	/0·10	/187	0·267	2·4	145	
26	*B*	15	0937	21·3	3·46/3·25	106	0·096/	0·017	/0·16	/084	0·245	2·7	150	
27	*A*	15	1056	35·9	2·34/2·30	139	0·086/	0·120	/0·09	/136	0·202	2·4	150	9

28	*D*	16	1720	18·6	/2·10	322			/0·12	/278	0·208	3·3	180	15
29	*B*	16	1901	38·5	1·47/1·82	093	0·093/				0·184	3·1		
30	*A*	16	2039	42·5	1·35/	354	0·025/	0·417			0·111	2·8		16
31	*C*	17	0904	35·5	6·85/7·32	184	0·241/0·357	0·024	/0·04	/145	0·510	3·1	202	
32	*C*	17	1104	42·5	7·42/8·10	186	0·266/0·426	0·011	/0·06	/130	0·673	3·5	192	12, 13
33	*A*	18	1110	39·8	5·12/	343	0·217/	−0·290			0·257	2·2		Tracking height 0·09 m. 12
34	*A*	18	1236	45·2	4·26/	004	0·165/	−0·620			0·216	1·9		Tracking height 0·10 m.
35	*A*	18	1352	42·5	2·54/3·15	036	0·110/0·078	−0·510			0·161	1·8		Tracking height 0·05 m. 15, 16
36	*A*	18	1455	20·0	2·52/2·62	067	0·108/0·049	−1·010			0·165	1·8		Tracking height 0·10 m. 14
37	*B*	18	1539	21·2	2·37/2·53	045	0·125/0·060	−0·316			0·101	2·4		

1. Run types include:
   A. 'Tracking'. All instruments in use with WF pressure in tracking mode.
   B. 'Calibration.' All instruments in use with WF pressure and other air-pressure sensors at common fixed height.
   C. 'Fixed height.' All instruments in use excepting WF instruments. Air-pressure sensors at different elevations.
   D. 'Nova only.' Only Nova instruments and wave staff in use.
   E. 'BIO only.' Only BIO instruments in use. No WF instruments.
   F. 'Wave-sensor comparison.' Wave staff clamped to Nova instrument package.
2. Start time in eastern standard time, December 1974.
3. Wind speed at 5 m elevation estimated on basis of logarithmic profile. First entry from sonic anemometer. Second entry from vertical cup anemometer array.
4. Direction of approach in degrees clockwise from north.
5. Ratio between measurement height and Monin-Obukhov length estimated from air/water temperature difference.
6. First entry is measured instantaneous drift at 0·5 to 1·5 m depth. Second entry is 'effective mean current' at spectral peak, computed in directional spectrum analysis (see §7).
7. Significant wave height from wave staff (four times root mean square).
8. Evaluated at spectral peak.
9. Problems with wave-follower pressure sensor.
10. Bimodal directional distribution.
11. Problems with BIO data tape.
12. Problems with Nova data tape.
13. Some rain. Possible blockage of pressure probe holes.
14. Upwind-travelling waves generated by Boston Whaler.
15. Wind speed variable.
16. Wind direction variable.

TABLE 2. Run summary.

wind upwind-travelling waves may have been inadvertently introduced by the 19 m *Calanus*.

Runs 15–21 were taken during a single frontal passage, and cover the most stable meteorological conditions encountered in the course of the experiment. The wind speed remained steady at 4 to 6 m s^{-1} and the wave field was aligned with the array. Unfortunately, the wave follower was seriously ill and unable to participate. The fixed sensors all operated properly, however, and much of the directional and unidirectional modelling has been carried out for these runs (see §§ 5 to 8). A short period of stable conditions with northeast winds occurred during a frontal passage on 18 December; runs 33 and 34 were taken during this period and, together with runs 3 and 4, are the best of the 'tracking' runs.

4. Preliminary data analysis

The preliminary analysis of data and later physical modelling were carried out in parallel at Bedford Institute (BIO data only) and at Nova University (the complete data set). In each case, the preliminary analysis was accomplished in several steps:

(1) translation of data tapes;

(2) cross-spectral analysis of high-speed data series; formation of the cross-spectral matrices;

(3) correction of these matrices for instrument response; other matrix conditioning; and

(4) analysis of low-speed data, including vertical-positioning analysis and wind-profile analysis.

The tape translations posed serious problems for both groups. The Bedford data tapes were played back, discriminated, filtered with phase-matched 11 Hz anti-aliasing filters and sampled at 20 Hz. After digitization, all series were converted to physical units (in the case of the sonic anemometer, axis rotation was also performed at this stage). Subsequent Fourier analysis produced some results at variance with corresponding Nova computations. This discrepancy was eventually traced to a problem with the in-house analog-to-digital converter at BIO which intermittently produced data-dependent errors in various bit lines causing spurious spikes, as a result of which a number of tapes had to be read a second time.

The Nova-tape translation was complicated by a tape-recorder malfunction which appeared midway in run 32 and persisted throughout the remainder of the experiment. As a result of this failure, one track on the digital data tapes (controlling the 1024 bit and the 16 bit) was continuously energized. Efforts to correct the resulting data series for this problem using a sliding linear predictor algorithm (Wiener 1949) met with considerable success, but because of differences in signal level the results of this analysis are somewhat uneven. Most low-speed signals (oversampled) were completely recovered. High-speed signals with r.m.s. levels smaller than or of the order of 16 bits were also completely recovered. All remaining signals were corrected for the 1024 bit, but not for the 16 bit; these signals contain a residual noise of (nominally) 8 bits r.m.s.

Cross-spectral estimates were computed at both BIO and Nova as follows: The data series were blocked (51·2 s = 1024 data points in the case of BIO; 40 s = 128, 256, 384, 768 data points, depending on signal, in the case of Nova) and Fourier transformed with an FFT algorithm (for block lengths of 384 and 768 data points, a second

less efficient algorithm was used). In the BIO analysis, the resulting complex Fourier coefficients were convolved with the weights $-0{\cdot}25$, $0{\cdot}5$, $-0{\cdot}25$ (equivalent to 'Hanning'–see Bingham, Godfrey & Tukey 1967). Cross-spectral estimates were then computed for each instrument pair by averaging products of Fourier coefficients over the data blocks. Thirty-two estimates in the frequency range of 0·0294 Hz to 1·2415 Hz resulted from the BIO analysis; 30 estimates in the range 0·025 Hz to 0·750 Hz resulted from the Nova analysis.

The cross-spectral analysis was summarized in the form of matrices containing the cross-spectral information between all instrument pairs. Subsequent conditioning of these matrices converts them to a form suitable for the modelling described in §§6 to 9. The principal modification is the correction for instrument response; a second modification relates to the interpretation of the wave-follower pressure measurements. We in effect interpret these measurements by converting them to 'equivalent' fixed measurements. The wave-induced pressure $p(t)$ at the sensing head is of the form

$$p(t) = P[\mathbf{x}_1, z_1 + h(t), t],$$

where $P(\mathbf{x}, z, t)$ is the wave-induced pressure field, $\mathbf{x}_1$ is the horizontal position of the pressure probe, z_1 is the (mean) tracking height, and $h(t)$ is the piston height. Expanding in Taylor series about $z = z_1$, we obtain

$$p(t) = P(\mathbf{x}_1, z_1, t) + h(t)\frac{\partial}{\partial z}P(\mathbf{x}_1, z_1, t) + \ldots.$$

Expanding in perturbation series (the zero-order field is the hydrostatic pressure) and equating terms of first order we obtain, correct to first order,

$$P(\mathbf{x}_1, z_1, t) = p(t) + s\rho g h(t), \tag{3}$$

where $s\rho$ is the air density, ρ is the water density and g is the gravitational acceleration. Equation (3) provides an algorithm for estimating the wave-induced pressure at a fixed elevation equal to the mean tracking height. We note in passing that this algorithm is entirely independent of the error signal $e(t)$, suggesting that quick response of the wave follower is not as important as one might imagine. Some lack of response is acceptable, even perhaps desirable; the important function of the wave follower is to keep the pressure head at small 'average' height above the instantaneous surface. This height must never be negative, but it need not be constant.

To recover $p(t)$ from the signal $k(t)$ recorded by the Kaman transducer [in order to compute P from (3)], several instrumental corrections, discussed in §2, are necessary. These include corrections for horizontal acceleration $H(t)$, vertical acceleration, and system response. These corrections and the conversion to an equivalent 'fixed' measurement are most conveniently effected in ω space. Let $\hat{P}$, $\hat{p}$, $\hat{K}$, $\hat{H}$ and $\hat{h}$ be (complex) Fourier amplitudes (all functions of ω) for P, p, K, H and h. Then to first order

$$\hat{K} = R_{Kp}\hat{p} + R_{KH}\hat{H} + R_{Kh}\hat{h},$$

where the (complex) responses R_{Kp}, R_{KH}, and R_{Kh} are functions of ω. System calibration [relation (2)] implies that R_{KH} is a real constant and that

$$R_{Kh} \simeq -r\omega^2 R_{Kp}.$$

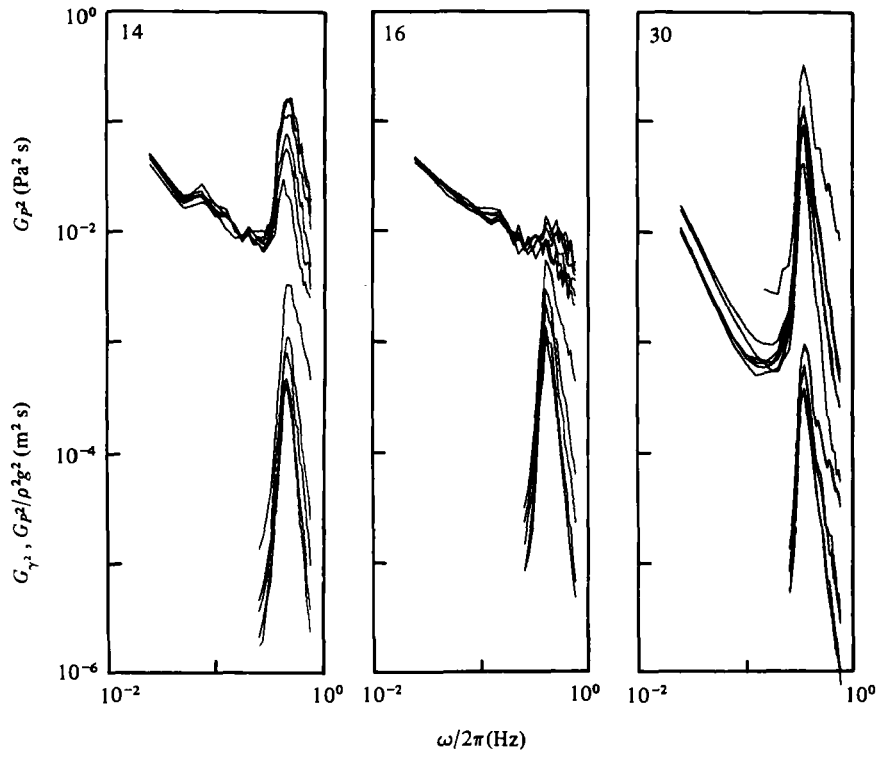

FIGURE 4. Air-pressure-sensor and wave-sensor autospectra for three representative runs.

It follows that

$$\hat{p} = \frac{1}{R_{Kp}}(\hat{K} - R_{KH}\hat{H}) + r\omega^2\hat{h}$$

and therefore

$$\hat{P} = \frac{1}{R_{Kp}}(\hat{K} - R_{KH}\hat{H}) + (s\rho g + r\omega^2)\hat{h}.$$

From this relation, we can derive a corresponding algorithm for computing the cross-spectrum between P and any other variable from the cross-spectra between K, H, h and the variable.

The diagonal elements of the cross-spectral matrix $G_{jl}(\omega)$ (that is, the wave sensor and the air pressure sensor auto spectra) are displayed in figure 4 for three representative runs. Runs 14 and 16 followed the cold front of 14 December. They are characterized by relatively high wind speeds from the design quadrant N–E. During run 14, the 11 m ketch *Catspaw* was positioned close by and downwind of the main array in order to backscatter waves. Run 30 was a low-wind-speed run with a large residual sea from the south. Note the large, well-defined wave-induced peak in the air-pressure spectra for runs 14 and 30. Characteristically, this peak is not nearly so well defined for run 16 (there are no upwind running waves).

Because the wave-follower pressure sensor exhibited some drift in sensitivity during the laboratory intercalibration, the field calibration runs, during which this sensor and the lower Elliott sensor were placed at the same elevation and close to one another, were examined for evidence of drift. Comparison with the lower Elliott sensor indicates that the response of the wave-follower pressure sensor was stable within $\pm 5\%$.

The extensive vertical position information contained in the Nova wave-sensor records and in the tide records was carefully examined in order to establish the instrument positions relative to the mean surface. Running averages of the wave-sensor records were constructed congruent with the tide records. Because the eastern-most wave sensor was fixed at the same absolute elevation during the entire experiment, direct comparison of its running average (which approximates the ensemble average $\langle\zeta\rangle$) with the signal T from the tide gauge provides a measure of the relative stability of the two instruments. Physical dimensions imply

$$\langle\zeta\rangle = T + 0{\cdot}60\,\mathrm{m}.$$

Linear regression of the full data set gives

$$\langle\zeta\rangle = 0{\cdot}992T + 0{\cdot}614\,\mathrm{m}.$$

The variance of the fit ($0{\cdot}00023\,\mathrm{m}^2$) is somewhat larger than would be expected from the resolution of the tide gauge, but is within design limits for the experiment.

The vertical positions of the other Nova wave sensors differed from run to run. During most runs, these positions were distinct; during 'calibration' runs they were visually adjusted to within 0·01 m of each other by lining up the air-pressure probes with the horizon. Comparison of wave sensor running averages during calibration runs revealed instrument drifts in excess of those monitored during the laboratory intercalibration. An independent measure of the vertical position of the wave sensors relative to the mean surface was computed by fitting autospectral elements to wave staff autospectral elements, assuming potential theory and zero mean current. These fits are not altogether convincing (it is not clear that even with a correction for mean current the spectra can be made to agree), and furthermore they yield vertical levels which often differ significantly from those obtained from the running averages. Ultimately, it was decided to base the vertical position of these instruments on running averages, using static calibration figures periodically adjusted for the drift implied by the calibration runs. We estimate the error in vertical position relative to the mean surface for the first three Nova instrument pairs to be 0·02 to 0·04 m; the corresponding error for the remaining instruments is 0·02 m.

Meteorological data included four high-speed series from BIO's sonic anemometer and four low-speed series of Nova's cup anemometers and vane. During digitization, the sonic anemometer series (two 'downwind' velocity components at 120°, a 'vertical' component and temperature) were converted to three Cartesian velocity components (a horizontal vector component $\mathbf{U}+\mathbf{u}$ and a vertical component w). By allowing for tilt, this conversion effects a zero mean in the vertical velocity component. The mean horizontal velocity at anemometer height $\mathbf{U}$, tangential stress $\boldsymbol{\tau} \equiv -s\rho\langle\mathbf{u}w\rangle$, and friction velocity $\mathbf{u}_*$ ($u_*u_* \equiv -\langle\mathbf{u}w\rangle$) were then estimated from time averages. Corresponding values for other variables, roughness length z_0, profile parameter Ω, mean horizontal velocity at 5 m elevation $\mathbf{U}_5$, and drag coefficient $C_5 = u_*^2/U_5^2$ were computed, assuming a logarithmic profile.

Independent estimates of $\boldsymbol{\tau}$, $\mathbf{u}_*$, z_0, Ω, $\mathbf{U}_5$, and C_5 were obtained from a least-squares analysis of the 45-minute time averages of the low-speed signals from the cup anemometer array. Discounting runs for which the wind direction placed the tower support upwind of the array, the resulting fits are reasonable (a two-parameter fit typically accounts for all three cup averages); nonetheless, the only parameter generally in good

agreement with the sonic value is $\mathbf{U}_5$ (stresses differ by as much as a factor of 2). No attempt has been made to rationalize this difference. Rather, we have elected to focus our subsequent model analysis (§5) on a meteorological parameter defined in terms of $\mathbf{U}_5$ and therefore essentially the same for both computations.

5. General discussion of the modelling of cross-spectral data

Further analysis is couched in terms of parametrizations of the atmospheric pressure field and the directional wave spectrum. The principal outputs of this analysis are estimates for the complex dimensionless ratio γ between wave-induced air pressure and surface elevation (in ω space), the directional wave spectrum $E_{\zeta^2}(\omega, \theta)$, the effective drift $\mathbf{D}(\omega, \theta)$, and an 'intrinsic' turbulent pressure spectrum $F_{Q^2}(\mathbf{k})$. In this section we describe the general structure of this analysis.

We assume that for each run the experimental data are appropriately summarized by the cross-spectral information between various instrument pairs in the main instrument array (the cross-spectral matrix), and by the corresponding mean meteorological and position information. Our object is to account for these data by

(1) constructing a physical model which relates the cross-spectral information to the mean meteorological and position information and to a finite number of (unknown) physical variables;

(2) estimating the physical variables by fitting the cross-spectral information to the model, typically by parametrizing the physical variables and effecting a least-squares minimization of the variance of the fit;

(3) assessing the extent to which the best fit model accounts for the data; and

(4) physically interpreting the best fit results.

Let $\zeta(\mathbf{x}, t)$ be the first order component of the surface elevation, and let $P(\mathbf{x}, z, t)$ and $Q(\mathbf{x}, z, t)$ be the first order wave-coherent and turbulent components of the pressure, respectively. Assuming stationarity and horizontal homogeneity, the second order statistics of these fields are defined by the covariances

$$C_{\zeta^2}(\boldsymbol{\xi}, \tau) \equiv \langle \zeta(\mathbf{x}, t)\, \zeta(\mathbf{x}+\boldsymbol{\xi}, t+\tau) \rangle,$$

$$C_{\zeta \mathrm{P}}(\boldsymbol{\xi}, z_2, \tau) \equiv \langle \zeta(\mathbf{x}, t)\, P(\mathbf{x}+\boldsymbol{\xi}, z_2, t+\tau) \rangle,$$

$$C_{\mathrm{P}^2}(\boldsymbol{\xi}, z_1, z_2, \tau) \equiv \langle P(\mathbf{x}, z_1, t)\, P(\mathbf{x}+\boldsymbol{\xi}, z_2, t+\tau) \rangle$$

and

$$C_{Q^2}(\boldsymbol{\xi}, z_1, z_2, \tau) \equiv \langle Q(\mathbf{x}, z_1, t)\, Q(\mathbf{x}+\boldsymbol{\xi}, z_2, t+\tau) \rangle,$$

or by their (one-sided) one-dimensional transforms

$$G_{\zeta^2}(\boldsymbol{\xi}, \omega) \equiv \frac{1}{\pi} \int_{-\infty}^{\infty} d\tau\, C_{\zeta^2} e^{-i\omega\tau},$$

$$G_{\zeta \mathrm{P}}(\boldsymbol{\xi}, z_2, \omega) \equiv \frac{1}{\pi} \int_{-\infty}^{\infty} d\tau\, C_{\zeta \mathrm{P}} e^{-i\omega\tau},$$

$$G_{\mathrm{P}^2}(\boldsymbol{\xi}, z_1, z_2, \omega) \equiv \frac{1}{\pi} \int_{-\infty}^{\infty} d\tau\, C_{\mathrm{P}^2} e^{-i\omega\tau},$$

and

$$G_{Q^2}(\boldsymbol{\xi}, z_1, z_2, \omega) \equiv \frac{1}{\pi} \int_{-\infty}^{\infty} d\tau\, C_{Q^2} e^{-i\omega\tau}$$

(the covariances $C_{\zeta Q}$ and $C_{\mathrm{P}Q}$ and their transforms vanish).

It follows from the linearity of the wave-coherent fields that the covariances C_{ζ^2}, $C_{\zeta P}$, and C_{P^2} may be written in terms of a single quantity, the spectral density of surface elevation (directional spectrum) $E_{\zeta^2}(\omega, \theta)$. Explicitly,

$$C_{\zeta^2} = \int_0^\infty d\omega \int_{-\pi}^{\pi} d\theta E_{\zeta^2} \cos(\mathbf{k}.\boldsymbol{\xi} - \omega\tau),$$

$$C_{\zeta P} = \rho_2 g \operatorname{Re}\left\{\int_0^\infty d\omega \int_{-\pi}^{\pi} d\theta \gamma_2 E_{\zeta^2} \exp[i(\mathbf{k}.\boldsymbol{\xi} - \omega\tau)]\right\}$$

and

$$C_{P^2} = \rho_1 \rho_2 g^2 \int_0^\infty d\omega \int_{-\pi}^{\pi} d\theta \gamma_1^* \gamma_2 E_{\zeta^2} \cos(\mathbf{k}.\boldsymbol{\xi} - \omega\tau)$$

from which it follows that for $\omega > 0$,

$$G_{\zeta^2} = \int_{-\pi}^{\pi} d\theta E_{\zeta^2} e^{-i\mathbf{k}.\boldsymbol{\xi}},$$

$$G_{\zeta P} = \rho_2 g \int_{-\pi}^{\pi} d\theta \gamma_2^* E_{\zeta^2} e^{-i\mathbf{k}.\boldsymbol{\xi}}$$

and

$$G_{P^2} = \rho_1 \rho_2 g^2 \int_{-\pi}^{\pi} d\theta \gamma_1 \gamma_2^* E_{\zeta^2} e^{-i\mathbf{k}.\boldsymbol{\xi}}.$$

In the above equations, ρ_j, is the zero order (mass) density evaluated at z_j, $j = 1, 2$. For $z_j < 0$,

$$\rho_j \simeq \rho \equiv 1035\,\mathrm{kg\,m^{-3}},$$

while for $z_j > 0$,

$$\rho_j \simeq s\rho \quad \text{where} \quad s \equiv 0{\cdot}0012.$$

Similarly, $\mathbf{k}(\omega, \theta)$ is the vector wavenumber (propagation vector) for the (ω, θ) component (in the absence of a mean current $\mathbf{k} = \mathbf{k}_0(\omega, \theta) \equiv (\omega^2/g)(\cos\theta, \sin\theta)$), and γ_j is the dimensionless pressure ratio defined by

$$\hat{P}_j = \rho_j g \gamma_j \hat{\zeta}, \tag{4}$$

where $\hat{\zeta}$ and $\hat{P}_j$ are (complex) amplitudes of surface elevation and wave-induced pressure (evaluated at z_j) for the (ω, θ) component. For $z_j < 0$, γ_j is the real function

$$\gamma_j = e^{\lambda_j},$$

where $\lambda_j \equiv kz_j$. For $z_j > 0$, γ_j is an unknown complex function γ of λ_j, ω, θ, and the wind profile. The function γ is the principal focus of the subsequent analysis. It is easy to show that for $\lambda_j = 0$,

$$\operatorname{Im}\gamma_j = s^{-1}\zeta_M = s^{-1}\omega^{-1}\beta_H,$$

where ζ_M is the 'growth rate' parameter defined by Miles (1957), and β_H is the 'growth rate' parameter used by Hasselmann (1960).

The choice of an appropriate parametrization of the wind profile dependence of γ is a crucial aspect of the data analysis. To the extent that the wind profile is logarithmic, we know that this profile and therefore γ are determined by three parameters (for example, vector friction velocity $\mathbf{u}_*$ and roughness z_0). While our analysis scheme is in principle capable of fixing the dependence of γ on three such parameters, we have

not attempted to do so. We doubt that our data, though extensive and relatively precise, are either sufficiently extensive or sufficiently precise to allow a stable determination of a three-parameter dependence. Accordingly, we have chosen to make our analysis in terms of a single parameter. Our choice of parameter is in part dictated by practical considerations and in part by a consideration of the structure of Miles' (1957) theory.

Miles' theory predicts that γ is a function of λ and of two dimensionless wind-profile parameters

$$\mu \equiv \frac{\mathbf{k}.\mathbf{U}_1}{\omega}$$

and

$$\Omega \equiv \frac{gk^2 z_0}{(\mathbf{k}.\mathbf{U}_1)^2},$$

where $\mathbf{U}_1 \equiv \mathbf{u}_*/\kappa$, and $\kappa = 0{\cdot}4$ is von Kármán's constant. Explicitly,

$$\mathrm{Re}\,\gamma(\mu, \Omega, \lambda) = \mu^2 \alpha(\mu, \Omega, \lambda)$$

and

$$\mathrm{Im}\,\gamma(\mu, \Omega, \lambda) = \mu^2 \beta(\mu, \Omega, \lambda),$$

α and β were computed as functions of μ for several representative values of ω and for $\lambda = 0$ by Miles (1959). Recent computations by Long (1980) extend these results to cover a range of Ω and λ values. We note that a second choice for the first parameter

$$\mu \equiv \frac{\mathbf{k}.\mathbf{U}(\epsilon k^{-1})}{\omega},$$

where $\mathbf{U}(z)$ is the mean velocity profile and ϵ is a constant of order 1 is equally convenient to the Miles theory. Both choices, however, require a more complete specification of the wind profile than is typically available.

The single most universal measure of the wind profile is the mean wind velocity at some reference level. In keeping with a desire to present results in a practical form and consistent with the previous analysis of Dobson (1971), Elliott (1972*b*) and Snyder (1974), we have accordingly chosen as our single parameter

$$\mu \equiv \frac{\mathbf{k}.\mathbf{U}_5}{\omega},$$

where $\mathbf{U}_5$ is the mean wind speed 5 m above the mean surface. Best fit results for $\gamma(\mu, \lambda)$ for a given data set will be taken as representative of an average value of Ω for that data set. We note in passing that our choice has the disadvantage that for given μ, Ω and λ, the prediction of the Miles theory is not unique, but requires the specification of a fourth parameter.

The presence of a mean current alters the above description of the wave field. Because of Newtonian invariance, we anticipate that in a frame of reference moving with the mean current, the physics are essentially unchanged (although the wind profile will no longer be simply logarithmic); however, it is not convenient to work in such a reference frame. Rather we shall attempt to modify our description in the fixed frame. We continue to interpret $E_{\zeta^2}(\omega, \theta)$ as the differential contribution to the mean square surface elevation for a wave component with radian frequency ω and direction of travel θ, as viewed from the fixed frame. There are two modifications. The first of

these has to do with the relationship between vector wavenumber $\mathbf{k}$ and (ω, θ). Let $\mathbf{D}(\omega, \theta)$ be the 'effective' mean current seen by the (ω, θ) component. The wavenumber $\mathbf{k}$ is determined by a suitably modified deep-water dispersion relation (the development is similar in water of intermediate depth)

$$(\omega - \mathbf{k}.\mathbf{D})^2 = gk. \tag{5}$$

As before, $\mathbf{k} = k(\cos\theta, \sin\theta)$ but k is now a function of $\mathbf{D}$. To determine this function, we rewrite (5) in the form

$$(k_0 - k\nu_0)^2 = kk_0, \tag{6}$$

where $\mathbf{k}_0 \equiv (\omega^2/g)\ (\cos\theta, \sin\theta)$

and

$$\nu_0 \equiv \frac{\mathbf{k}_0.\mathbf{D}}{\omega}.$$

Expanding k in powers of ν_0 and substituting into (6), we obtain

$$k = k_0(1 - 2\nu_0 + 5\nu_0^2 + \ldots).$$

[Note also that for $\nu \equiv \mathbf{k}.\mathbf{D}/\omega$ and $\mu_0 \equiv \mathbf{k}_0.\mathbf{U}_5/\omega$

$$\nu = \nu_0(1 - 2\nu_0 + 5\nu_0^2 + \ldots)$$

and

$$\mu = \mu_0(1 - 2\nu_0 + 5\nu_0^2 + \ldots).]$$

The analysis in §7 is based on truncating this expansion after three terms.

The second modification concerns the parametrization of γ. Because of Newtonian invariance we anticipate that γ will properly be a function of the parameter

$$\frac{\mathbf{k}.(\mathbf{U}_5 - \mathbf{D})}{\omega - \mathbf{k}.\mathbf{D}} = \frac{\mu - \nu}{1 - \nu} = \mu + (\mu - 1)\nu + \ldots.$$

For $|\nu| \ll |\mu|$ and $\mu \sim 1$, the new parameter reduces to μ. We will in fact, with some attendant biasing of results for $\mu > 2$ and $\mu < 0$, assume the two parameters to be generally equal (see §9).

The above discussion identifies the physical variables which determine the cross-spectral quantities G_{ζ^2}, $G_{\zeta P}$, and G_{P^2}. These variables are the directional spectrum $E_{\zeta^2}(\omega, \theta)$, the 'effective' mean current $\mathbf{D}(\omega, \theta)$, and the dimensionless wave-induced atmospheric pressure profile $\gamma(\mu, \lambda)$. In §8, we will similarly relate the remaining cross-spectral quantity G_{Q^2} to a forth physical variable, the 'intrinsic' spectrum of turbulent atmospheric pressure $F_{Q^2}(\mathbf{k})$.

In order to complete our physical model of the matrix of cross-spectral estimates $G_{jl}(\omega)$ between instrument pairs, we need only relate these estimates to G_{ζ^2}, $G_{\zeta P}$, G_{P^2}, and G_{Q^2}. Let $G_{jl}(\omega)$ be a one-sided estimate for instrument j and instrument l, and let $\boldsymbol{\xi}_{jl} \equiv \mathbf{x}_l - \mathbf{x}_j$. Then

$G_{jl}(\omega) = G_{\zeta^2}(\boldsymbol{\xi}_{jl}, \omega)$, wave-staff/wave-staff elements,

$G_{jl}(\omega) = G_{\zeta P}(\boldsymbol{\xi}_{jl}, z_l, \omega)$, wave-staff/water-pressure-sensor elements, and wave-staff/air-pressure-sensor elements,

$G_{jl}(\omega) = G_{P^2}(\boldsymbol{\xi}_{jl}, z_j, z_l, \omega)$, water-pressure-sensor/water-pressure-sensor elements and water-pressure-sensor/air-pressure-sensor elements,

j \ l	Surface elevation	Water pressure	Air pressure
Surface elevation	1	$\rho g e^{\lambda_l}$	$s\rho g\gamma^*(\mu, \lambda_l)$
Water pressure	$\rho g e^{\lambda_j}$	$(\rho g)^2 e^{\lambda_j+\lambda_l}$	$s(\rho g)^2 e^{\lambda_j}\gamma^*(\mu, \lambda_l)$
Air pressure	$s\rho g\gamma(\mu, \lambda_j)$	$s(\rho g)^2\gamma(\mu, \lambda_j)\, e^{\lambda_l}$	$(s\rho g)^2\gamma(\mu, \lambda_j)\,\gamma^*(\mu, \lambda_l)$

TABLE 3. Weight function $R_{jl}(\mu, \lambda_j, \lambda_l)$.

and

$$G_{jl}(\omega) = G_{P^2}(\boldsymbol{\xi}_{jl}, z_j, z_l, \omega) + G_{Q^2}(\boldsymbol{\xi}_{jl}, z_j, z_l, \omega),$$

air-pressure-sensor/air-pressure-sensor elements.

In each case, the first term on the right reduces to expressions of the form

$$\int d\theta R_{jl} E_{\zeta^2} \exp[-i\mathbf{k}.\boldsymbol{\xi}_{jl}],$$

where the weight function $R_{jl}(\mu, \lambda_j, \lambda_l)$ is tabulated in table 3.

In the next three sections, we will exploit the relationship between the cross-spectral matrix elements and the variables E_{ζ^2}, $\mathbf{D}$, γ, and F_{Q^2} in order to obtain estimates of these variables. In §6, we will make several simplifying assumptions for the θ dependence of E_{ζ^2} which will allow us to estimate E_{ζ^2} and γ from wave-staff/wave-staff and wave-staff/Elliott air-pressure-sensor matrix elements. In §7, we will develop parametrizations of E_{ζ^2} and D which will allow us to estimate these variables from wave-sensor/wave-sensor matrix elements. We will then use wave-sensor/air-pressure-sensor matrix elements to estimate γ. A special analysis will be required for the upwind-travelling portion of E_{ζ^2}, because typically it cannot be resolved from wave sensor/wave sensor elements. Finally in §8, we will use air-pressure-sensor/air-pressure-sensor matrix elements to estimate F_{Q^2}.

6. The wave-induced pressure field: simplified model

A simplified algorithm for estimating the wave-induced atmospheric pressure profile can be obtained by assuming a specific directional dependence for E_{ζ^2}; this approach was used by Dobson (1971) and Elliott (1972*b*) to interpret their previous data. E_{ζ^2} will be taken to be of the form

$$E_{\zeta^2}(\omega, \theta) = E_{\zeta^2}(\omega)\,\psi[\theta - \phi(\omega)],$$

where the principal wave azimuth $\phi(\omega)$ is known and $\psi(\theta)$ is given by either (unidirectional case)

$$\psi(\theta) \equiv \delta(\theta)$$

or

$$\psi(\theta) \equiv \frac{2}{\pi}\cos^2\theta, \quad |\theta| \leqslant \frac{\pi}{2}$$

$$\equiv 0, \quad |\theta| > \frac{\pi}{2}.$$

In both cases, we assume

$$\mathbf{D}(\omega, \theta) = 0.$$

$\Theta-\phi$	$\hat{\mu}_0/\mu_0$
0	0·85
10	0·84
20	0·80
30	0·74
40	0·65

TABLE 4. $\hat{\mu}_0/\mu_0$ as a function of $(\Theta-\phi)$ assuming $\cos^2(\theta-\phi)$ spreading (see text).

In the first case, wave-staff/wave-staff matrix elements take the form

$$G_{jl}(\omega) = E_{\zeta^2}(\omega)\exp[-i\mathbf{k}_0.\boldsymbol{\xi}_{jl}],$$

while wave-staff/air-pressure-sensor elements take the form

$$G_{jl}(\omega) = s\rho g\gamma^*(\mu_0, k_0 z_l)\, E_{\zeta^2}(\omega)\exp[-i\mathbf{k}_0.\boldsymbol{\xi}_{jl}].$$

Here
$$\mathbf{k}_0(\omega) \equiv \frac{\omega^2}{g}[\cos\phi(\omega), \sin\phi(\omega)]$$

and
$$\mu_0(\omega) \equiv \frac{\mathbf{k}_0(\omega).\mathbf{U}_5}{\omega}.$$

If follows that for the lth air-pressure sensor and jth wave staff,

$$\gamma(\mu_0, k_0 z_l) = \frac{1}{s\rho g}\frac{G^*_{jl}(\omega)}{G_{jj}(\omega)}\exp[-i\mathbf{k}_0.\boldsymbol{\xi}_{jl}]. \tag{7}$$

In the second case, it is not possible to carry out the corresponding integrations without knowing more about the μ dependence of γ. From the mean-value theorem one can derive the approximate result

$$\gamma(\hat{\mu}_0, k_0 z_l) \simeq \frac{1}{s\rho g}\frac{G^*_{jl}(\omega)}{G_{jj}(\omega)}\exp[-i\mathbf{k}_0.\boldsymbol{\xi}_{jl}], \tag{8}$$

where
$$\hat{\mu}_0(\omega) \equiv \int_{-\pi}^{\pi} d\theta\mu\psi[\theta-\phi(\omega)].$$

If the wind direction Θ coincides with $\phi(\omega)$ this integral reduces to $\hat{\mu}_0 = (8/3\pi)\mu_0$. If not, $\hat{\mu}_0$ is even smaller (see table 4). Because the principal difference between relations (6) and (7) is the change of scale for μ, a single data analysis is sufficient to determine the results for either algorithm.

This analysis has been carried out for a number of runs using data from the BIO wave staff and from the two Elliott air-pressure sensors. The latter were separated vertically by 0·5 to 1·5 m, with the lower sensor 0·5 to 1 m above the mean water surface. The cross-wind horizontal separation between the wave staff and the air-pressure sensors was typically less than 0·3 m.

For each run, the mean direction of travel in each frequency band $\phi(\omega)$ was obtained from the directional spectrum analysis described in §7. In runs 15 to 20, there is a single dominant peak for which the wind and wave azimuth differ by about 20° (see table 2); at higher frequencies the wave azimuth tends more towards the wind azimuth. This tendency is used to extrapolate to shorter wavelengths where the directional

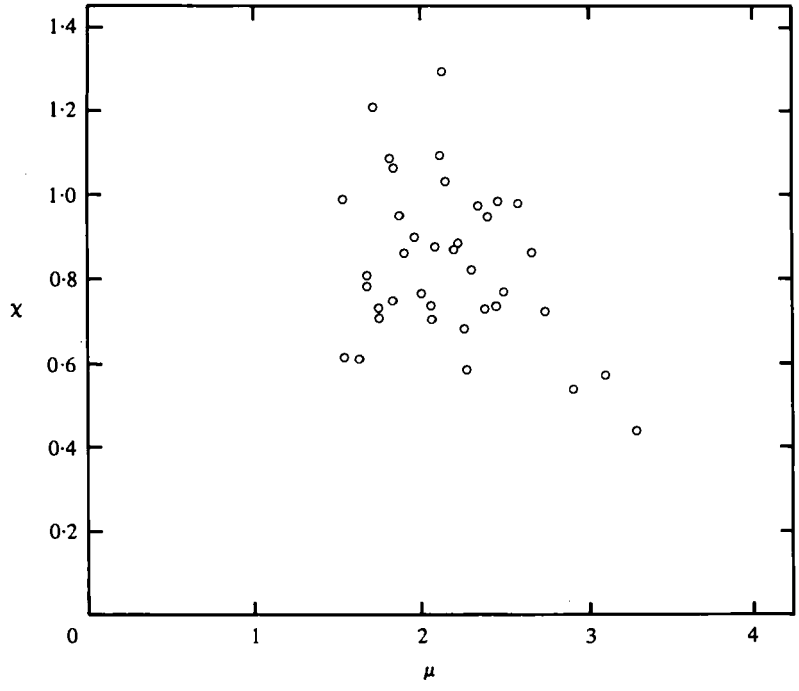

FIGURE 5. $\chi(\mu)$ for runs 15 to 20; simplified analysis.

spectrum analysis is unreliable. For some of the other Bight runs there is more than one peak. In this case the wave azimuth is taken to be a weighted mean of the larger peaks. The appropriate wave azimuth is then used to correct for the sensor separation phase shift [the exponential factor in (7)]; the uncertainty in the correction for the phase shift is estimated to be less than $\pm 5°$ and is largest at the high frequencies.

Further analysis has been directed towards extrapolating the resulting estimates for γ to the mean water surface ($\lambda = 0$) and estimating the corresponding momentum transfer. The quantity γ is assumed to be of the form

$$\gamma(\mu, \lambda) = \gamma(\mu)\, e^{-\chi(\mu)\lambda}$$

with $\gamma(\mu)$ complex and $\chi(\mu)$ real. Implicit in this assumption is the constraint that the phase of γ is independent of λ (see Elliott 1972*b*; and Snyder 1974). An estimate for $\chi(\mu)$ is given by

$$\chi(\mu) = \frac{1}{\lambda_2 - \lambda_1} \ln \left| \frac{\gamma(\mu, \lambda_1)}{\gamma(\mu, \lambda_2)} \right|,$$

where the subscripts 1 and 2 denote respectively the lower and upper pressure sensors. The estimates for $\chi(\mu)$ shown in figure 5 are limited to the high wind-speed group, runs 15 to 20, over the range $1 < \mu < 3$. The reason for this restriction is that for much of the high frequency and low wind-speed data the coherence level between surface elevation and upper air pressure is so low as to make the data unreliable. Only data for which the phase between surface elevation and air pressure for the lower sensor is within $\pm 15°$ of its value for the upper sensor are included in the analysis. Although there is some indication that $\chi(\mu)$ decreases with increasing μ, the scatter in figure 5 is

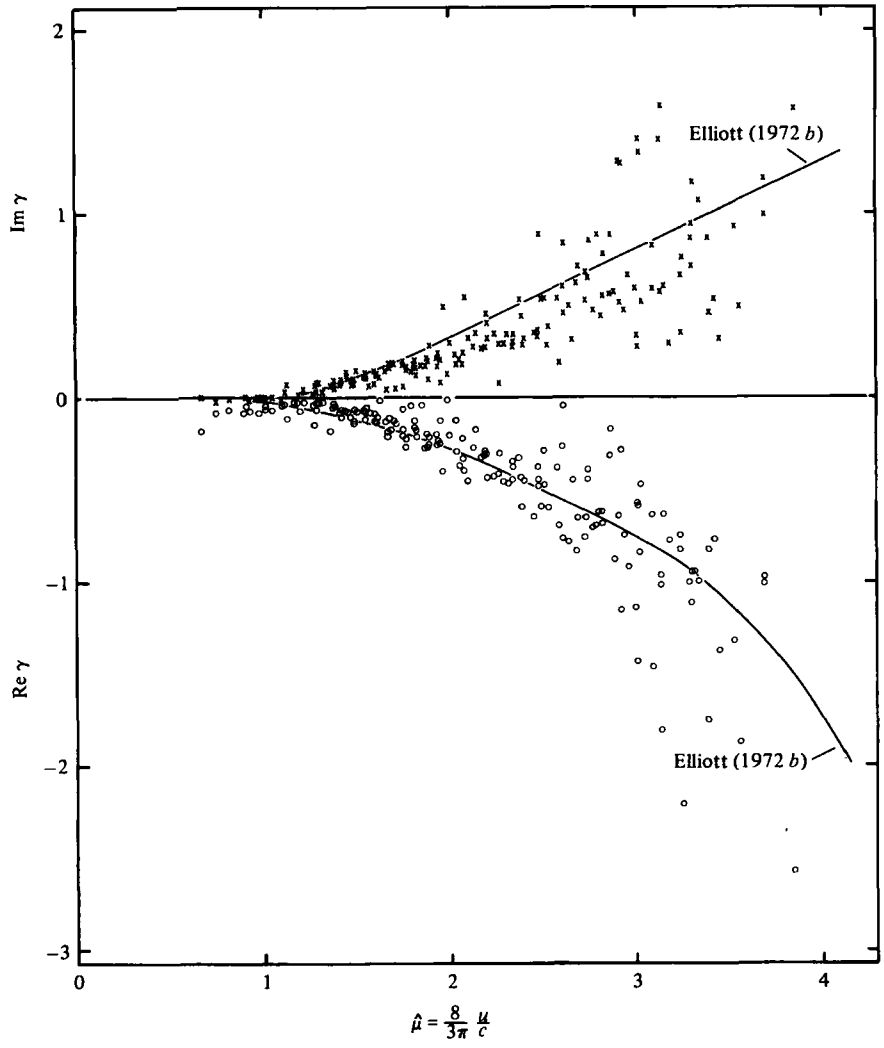

FIGURE 6. $\gamma(\mu, 0)$ for runs 5, 15 to 23 and 25; simplified analysis. ×, Im γ; ○, Re γ.

sufficient to make an estimate of the trend unreliable. For the present data we find $\chi = 0{\cdot}86 \pm 0{\cdot}21$, as compared with Elliott's (1972) data for which $\chi = 0{\cdot}83 \pm 0{\cdot}22$. (We note in passing that not all of the above decrease in decay rate (relative to potential theory) can be attributed to the dynamics of the growth mechanism. A second, perhaps dominant, cause for this decrease is the Doppler shift associated with the mean drift current. This shift effectively reduces the wavenumber associated with a given frequency by a factor of $1 - \nu$, where ν is the drift to phase speed ratio defined in §5.)

Setting $\chi = 0{\cdot}86$, $\gamma(\mu, 0)$ was extrapolated from $\gamma(\mu, \lambda_1)$ for runs 15 to 20 and for runs 5, 21, 22, 23 and 25 (figure 6). Characteristically these results are reasonably well defined for $\hat{\mu}_0 < 3$, with increasing scatter for $\hat{\mu}_0 > 3$. The solid line in the figure is a mean curve through the Elliott (1972) data points, re-analysed using the same extrapolation techniques as for the BOA data; the agreement is excellent.

A comparison between the lower Elliott sensor extrapolated to mean tracking height using $\chi = 0{\cdot}86$, and the wave-follower pressure sensor, corrected as described

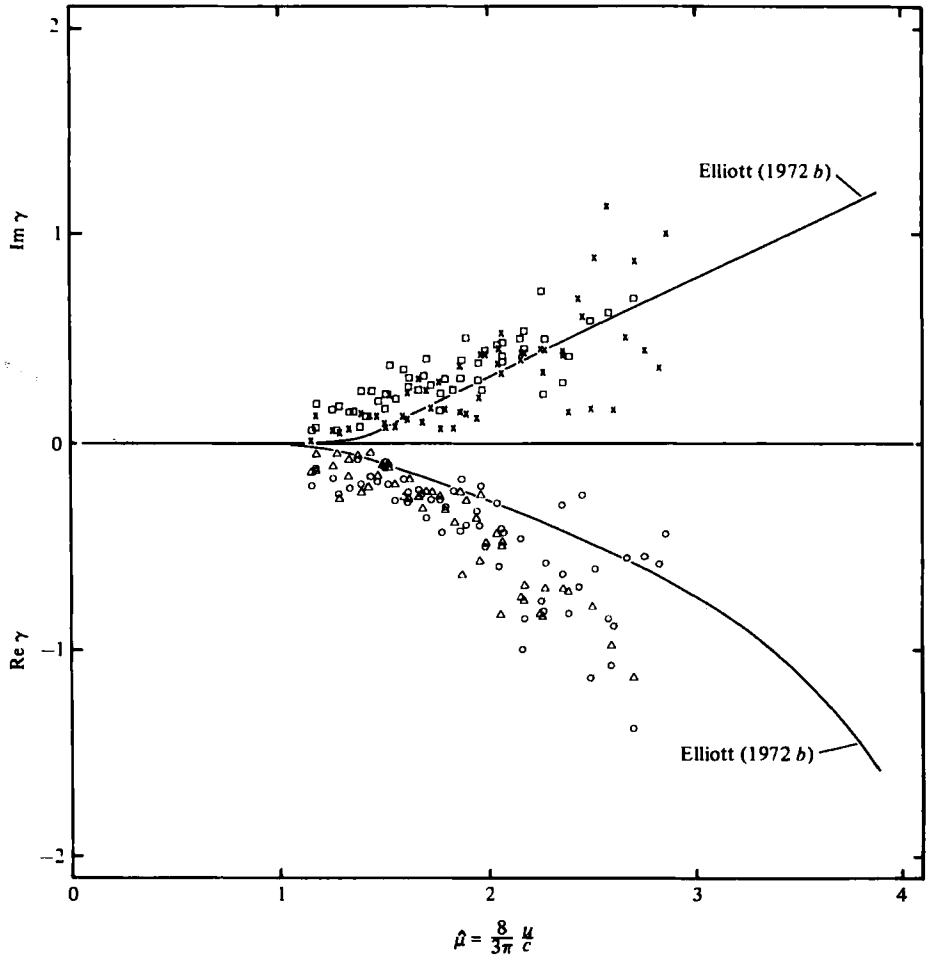

FIGURE 7. $\gamma(\mu, 0)$ for runs 4, 7, 33 and 34; simplified analysis. ×, ○, fixed sensors; □, △, wave follower.

in §4, is shown in figure 7 for tracking runs 4, 7, 33, and 34. As is evident from the figure, the agreement between the sensors is reasonable, except perhaps at $\mu \simeq 1$ where the Im γ values from the wave follower slightly exceed those from the fixed sensors. The BOA curves do not agree so well with the reworked Elliott (1972*b*) curves as for the case of the 'best' data set of figure 6. In particular the wave follower Im γ points generally lie above the Elliott (1972*b*) line for $\hat{\mu}_0 < 2$, and the BOA Re γ values are more negative than the Elliott values at a given $\hat{\mu}_0$.

7. The wave-induced pressure field: general model

The analysis of the previous section was based on the assumption of a specific form for the directional dependence of E_{ζ^2}. Also, the effect of the mean current **D** on dispersion was neglected. The more general analysis described in this section, which has the same goals as a similar modelling attempt by Snyder (1974) but differs greatly in the means used to achieve the goals, consists of three distinct parts:

(1) estimation of $E_{\zeta^2}(\omega, \theta)$ and $\mathbf{D}(\omega, \theta)$ for each run,

(2) estimation of $\gamma(\mu, \lambda)$ for $\mu > 0$,

(3) re-estimation of $E_{\zeta^2}(\omega, \theta)$ for each backscatter run, and of $\gamma(\mu, \lambda)$ for $\mu < 0$.

The first and third analyses are iterative computations in which each variable is alternatively used to improve the estimate of the other.

To effect the first analysis, we expand $E_{\zeta^2}(\omega, \theta)$ in the form

$$E_{\zeta^2}(\omega, \theta) = \sum_n^N {}_nE_{\zeta^2}(\omega)\, \psi_n(\theta - \phi) \quad \text{for linear analysis,}$$

or

$$E_{\zeta^2}(\omega, \theta) = (\sum_n^N {}_nE_{\zeta^2}(\omega)\, \psi_n(\theta - \phi))^2 \quad \text{for bilinear analysis.} \tag{9}$$

The latter analysis ensures that the best fit E_{ζ^2} is everywhere positive. The principal direction ϕ is set equal to the wind azimuth and is independent of ω. Several choices of basis set $\psi_n(\theta)$ are employed, most commonly (with $m = 1$) the set

$$\begin{aligned} \psi_n(\theta) &\equiv \cos^m\theta \cos(n-1)\theta, \quad |\theta| < \tfrac{1}{2}\pi, \quad n \text{ odd} \\ &\equiv \cos^m\theta \sin n\theta, \quad |\theta| < \tfrac{1}{2}\pi, \quad n \text{ even} \\ &\equiv 0, \quad |\theta| > \tfrac{1}{2}\pi \end{aligned} \tag{10}$$

which does not allow wave components travelling against the wind.

It is assumed that $\mathbf{D}(\omega, \theta)$ is adequately represented by the deep water weighting

$$\mathbf{D} = k_0 \int_{-\infty}^{0} dz\, e^{k_0 z} \mathbf{U}(z),$$

where $\mathbf{U}(z)$ is the mean velocity profile. Note that this weighting (essentially a zero order iteration of the more general weighting with k substituted for k_0) makes $\mathbf{D}$ independent of θ. Expanding $\mathbf{U}$ in Taylor series

$$\mathbf{U}(z) = \sum_p^P \mathbf{U}_p z^p$$

generates a representation for $\mathbf{D}$ for the form

$$\mathbf{D} = \sum_p^P D_p(\omega)\, \mathbf{U}_p, \tag{11}$$

where

$$D_p(\omega) \equiv k_0 \int_{-\infty}^{0} dz\, z^p e^{k_0 z} = (-1)^p (p-1)!\, k_0(\omega)^{-p}.$$

The parametrizations (9) and (11) determine the spectral matrix of wave sensors (surface elevation and water pressure sensors) as functions of the parameters ${}_nE_{\zeta^2}(\omega)$ and $\mathbf{U}_p$. The corresponding matrix elements are linear or bilinear functions of the ${}_nE_{\zeta^2}(\omega)$ and nonlinear functions of the $\mathbf{U}_p$. To estimate the best fit value for these parameters, we initialize

$$\mathbf{D}^{(0)}(\omega) = 0$$

and calculate $E_{\zeta^2}{}^{(q)}(\omega, \theta)$, frequency band by frequency band, from $D^{(q-1)}(\omega)$ by minimizing the variance (linear analysis)

$$V^{(q)}(\omega) \equiv \sum_{jl} \left| G_{jl}(\omega) - \sum_n^N H_{jl_n}^{(q-1)}(\omega)\, {}_nE_{\zeta^2}{}^{(q)}(\omega) \right|^2$$

Band†	$\mathbf{D}^{(4)}(\omega)$‡ (m s^{-1})	$V^{(1)}(\omega)$ (10^{-9} m^2)	$V^{(4)}(\omega)$ (10^{-9} m^2)
15	0·04/0·10	3·7	3·3
16	0·08/0·10	15·2	6·3
17	0·11/0·10	21·6	11·1
18	0·14/0·10	33·1	4·3
19	0·17/0·10	20·0	7·3
20	0·19/0·10	9·0	2·3
21	0·21/0·10	3·9	1·7
22	0·23/0·10	1·5	0·7
23	0·24/0·10	1·4	1·1

† Frequency interval is 0·025 Hz.
‡ First entry is downwind component; second entry is crosswind component.

TABLE 5. Effective mean current $\mathbf{D}^{(4)}(\omega)$, run 16. Estimated from directional spectrum analysis.

or the variance (bilinear analysis)

$$V^{(q)}(\omega) \equiv \sum_{jl} \left| G_{jl}(\omega) - \sum_{m}^{M} \sum_{n}^{N} H_{jlnm}^{(q-1)}(\omega)\, {}_{m}E_{\xi}^{(q)}(\omega)\, {}_{n}E_{\xi}^{(q)}(\omega) \right|^2$$

with respect to the real coefficients ${}_{n}E_{\xi}^{(q)}(\omega)$. Here

$$H_{jln}^{(q)} \equiv \int_{-\pi}^{\pi} d\theta\, R_{jl}^{(q)} \psi_n \exp[-i\mathbf{k}^{(q)}.\boldsymbol{\xi}_{jl}]$$

and

$$H_{jlmn}^{(q)} \equiv \int_{-\pi}^{\pi} d\theta\, R_{jl}^{(q)} \psi_m \psi_n \exp[-i\mathbf{k}^{(q)}.\boldsymbol{\xi}_{jl}],$$

where the $R_{jl}^{(q)}$ are defined by table 3. (Typically, the early iterations employ the linear form and the final interations ($q = 3, 4$) the bilinear form.) $\mathbf{D}^{(q)}(\omega)$ is in turn estimated by minimizing the integral variance (the integral runs over the frequency bands of the spectral analysis)

$$V^{(q)} \equiv \sum_{jl} \int d\omega \left| G_{jl}(\omega) - H_{jl}^{(q)}(\omega) \right|^2$$

with respect to the real coefficients $\mathbf{U}_{p}^{(q)}$.

Here

$$H_{jl}^{(q)} \equiv \int_{-\pi}^{\pi} d\theta\, R_{jl}^{(q)}\, E_{\xi}^{(q)} \exp[-i\mathbf{k}^{(q)}.\boldsymbol{\xi}_{jl}].$$

The dependence on $\mathbf{U}_{p}^{(q)}$, through relations (5) and (11), is implicit in $\mathbf{k}^{(q)}$ and therefore in $R_{jl}^{(q)}$. A Newton–Raphson technique is employed to effect the minimization. Typically, this minimization is constrained so that for $p \geqslant 1$, $\mathbf{U}_p$ has the direction ϕ. A constraint of this form is normally required for stability because the matrix elements are comparatively insensitive to the cross-wave component of $\mathbf{D}$ [k is a function of the dot product $\nu_0 \equiv (\mathbf{k}_0.\mathbf{D})/\omega$]. By leaving $\mathbf{U}_0$ unconstrained, some cross-wave (tidal) flow is allowed. Resulting estimates for $\mathbf{D}(\omega, \theta)^{(4)}$, $P = 1$, are shown in table 5 for run 16. Note that, as would be anticipated, the downwind component of $\mathbf{D}$ is of order 0·0 to 0·3 m s^{-1}, is positive, and is an increasing function of frequency. Also shown in

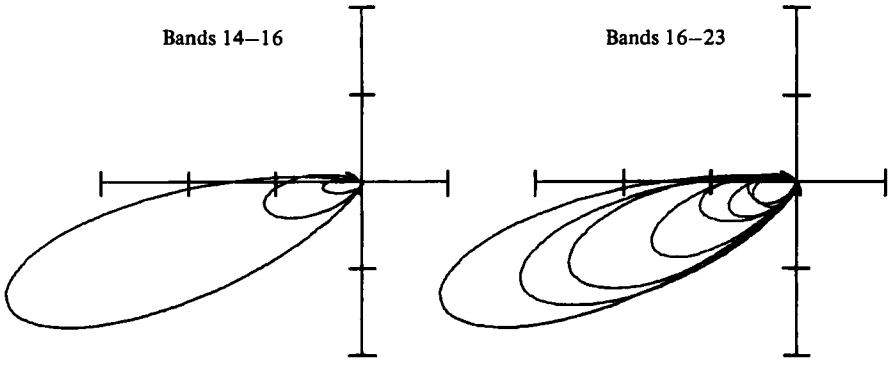

FIGURE 8. Directional spectrum for run 16. Bilinear analysis with $N = 5$. Scale is 0·002 m² s per division.

the table are the variances $V^{(1)}(\omega)$ and $V^{(4)}(\omega)$. Clearly, allowance for a mean current has improved the directional spectrum computation. The corresponding final estimate for E_{ζ^2} is displayed in figure 8. Note the shift in principal direction with frequency which results from the asymmetric fetch distribution of the Bight site in easterly winds.

To effect the second analysis, we expand

$$\gamma(\mu, \lambda) = \sum_{rs}^{RS} \Gamma_{rs} \mu^r L_s(\lambda) \quad \text{for linear analysis,}$$

or

$$\gamma(\mu, \lambda) = \sum_{q}^{Q} \Gamma_q \mu^q \sum_{rs}^{RS} \Lambda_{rs} \mu^r L_s(\lambda) \quad \text{for bilinear analysis.}$$

The coefficients Γ_{rs} and Γ_q are complex and the coefficients Λ_{rs} real; in the bilinear case the phase of γ is independent of λ. Two choices for $L_s(\lambda)$ are employed. One choice is the set (related to the Laguerre polynomials)

$$L_s(\lambda) \equiv \lambda^s e^{-\lambda}.$$

The second choice is the set of empirical orthogonal functions recently computed by Long (1980) from a set of theoretical pressure profiles calculated according to the Miles (1957) theory. The Long–Miles functions have one very desirable property, which is that it is possible to represent accurately the λ dependence of the solutions of the Miles theory (and of potential theory) over a wide range of μ and Ω by superimposing only a few functions. Two of these functions account for 99·98 % of the variance about zero of the set of theoretical pressure profiles used in the empirical orthogonal function computation.

Given $E_{\zeta^2}(\omega, \theta)$ and $\mathbf{D}$ (ω, θ), these parametrizations determine the cross-spectral matrix between wave sensors and air-pressure sensors. The corresponding matrix elements are linear functions of the coefficients Γ_{rs} (linear analysis) or bilinear functions of the coefficients Γ_q and Λ_{rs} (bilinear analysis). The best fit estimates for these coefficients are determined by minimizing the variance (linear analysis)

$$V \equiv \sum_{jl} \sum \int_0^\infty d\omega M_{jl}(\omega)^2 \left| G_{jl}(\omega) - \sum_{rs} I_{jlrs}(\omega) \Gamma_{rs}^* \right|^2$$

with respect to the γ_{rs}, or the variance (bilinear analysis)

$$V = \sum\sum_{jl} \int_0^\infty d\omega M_{jl}(\omega)^2 |G_{jl}(\omega) - \sum_{qrs} I_{jl(q+r)s}(\omega)\Gamma_q^* \Lambda_{rs}|^2$$

with respect to the Γ_q and Λ_{rs}.

In either case, the unlabelled sum extends over a group of runs as small as a single run or as large as the entire data set; $M_{jl}(\omega)$ is a masking (weight) function used to eliminate less reliable cospectral values from widely separated instruments. Typically

$$\begin{aligned} M_{jl}(\omega) &\equiv [G_{jj}(\omega)\, G_{ll}(\omega)]^{-\frac{1}{2}} \quad \text{for} \quad k_0(\omega)\,\xi_{jl} < \phi_0 \\ &\equiv 0 \quad \text{otherwise,} \end{aligned}$$

where ϕ_0 is some phase cut-off. Finally, I_{jlrs} is given by

$$I_{jlrs} \equiv s(\rho g)^2 \int_{-\pi}^{\pi} d\theta e^{\lambda_j} E_{\zeta^2} \mu^r L_s \exp[-i\mathbf{k}.\boldsymbol{\xi}_{jl}].$$

These minimizations have typically been subjected to two constraints: a potential-theory constraint, and a uniqueness constraint (bilinear analysis only). The potential theory constraint requires that

$$\gamma(0, \lambda) = -e^{-\lambda}.$$

For the Laguerre-related polynomials, this constraint takes the form

$$\Gamma_{00} = -1$$

and

$$\Gamma_{0s} = 0, \quad s > 0 \quad \text{for linear analysis,}$$

or

$$\Gamma_0 = 1, \quad \Lambda_{00} = -1$$

and

$$\Lambda_{0s} = 0, \quad s > 0 \quad \text{for bilinear analysis.}$$

For the Long–Miles functions, the constraint takes the form

$$\Gamma_{0s} = N_s \quad \text{for linear analysis,}$$

or

$$\Gamma_0 = 1$$

and

$$\Lambda_{0s} = N_s \quad \text{for bilinear analysis.}$$

The N_s are the coefficients for the expansion of $-e^{-\lambda}$ in Long–Miles functions. For the bilinear analysis, the uniqueness constraint further requires that

$$\Lambda_{r0} = 0, \quad r > 0.$$

It is not appropriate here to describe the details of the numerical computations required in order to effect the above minimizations. The details have been worked out consistent with an overall system for geophysical data management and analysis; the minimizations are feasible and have meaning but there are practical limits to the power of the analysis. Without a theory of the errors inherent in the computations, it is not possible at the outset to completely foresee what course they will take; much has to be worked out on a trial and error basis. The basic dilemma is a familiar one: statistical noise in the spectral estimates and (most probably) basic inadequacies in the theoretical model combine to limit the resolution of the computation. As the

number of degrees of freedom increases, the variance decreases rapidly, then levels off. Concurrently, 'unreasonable' fits become 'reasonable', then again 'unreasonable'.

As a test of the general model, the 1970 data from the Bight of Abaco (Snyder 1974) were re-analysed using an abbreviated version of this model. The average 'surface normalized' spectral matrices previously computed by Snyder (representing different wind speeds) were corrected for the calibration error discussed in §2. A directional spectrum $E_{\zeta^2}(\omega, \theta)$ and mean current $\mathbf{D}(\omega, \theta)$ were calculated for each matrix from wave-sensor/wave-sensor elements. [The basis (10) with $m = 1$ and $N = 3$ was used to represent E_{ζ^2}.] Both E_{ζ^2} and $\mathbf{D}$ were in good agreement with previous estimates. The growth-rate parameter, γ, was then estimated for a Laguerre basis, linear fit, with potential theory constraint ($R = 3, S = 0$). The results of this analysis are shown in figure 9, superimposed on a corrected version of Snyder's figure 14. We note that the general model gives results in reasonable agreement with the simpler analysis, although it tends to predict a somewhat larger $|\mathrm{Re}\,\gamma|$. This discrepancy probably results from the neglect of upwind-travelling waves, which were known to be present during the 1970 experiments. These waves contribute significantly to wave-sensor/air-pressure-sensor matrix elements, producing an elevated estimate for $|\mathrm{Re}\,\gamma|$ (assuming the phase of the upwind-travelling waves to be $\sim 180°$).

A full-blown version of the general model was next applied to runs 15 to 20 of the present data. Tables 6 and 7 list the proportional variance in the linear and bilinear fits. Figures 10 and 11 show the corresponding variation in the best fit $\gamma(\mu, 0)$ and $\gamma(2, \lambda)$ for the Long–Miles basis, linear fit, with potential theory constraint; examination of the differences between observed and best-fit cross-spectral estimates, instrument pair by instrument pair (including both BIO and Nova instrument pairs), suggests that the differences are random with no significant systematic trends.

Some indication of the confidence limits of the best-fit analysis or of the physical variation in γ is obtained by performing the analysis run by run. Figures 12 and 13 show the corresponding variation in $\gamma(\mu, 0)$ and $\gamma(2, \lambda)$ for runs 15 to 20 (individual analyses), Long–Miles basis, bilinear fit, with potential theory constraint and $Q = 2, R = 1, S = 1$.

Finally, figures 14 and 15 show $\gamma(\mu, \lambda)$ for runs 15 to 20 (bulk analysis), Long–Miles basis, linear and bilinear fits, respectively, with potential-theory constraint. Consistent with Elliott (1972*b*) and with the simplified analysis of the previous section, the latter fits suggest a near exponential dependence on λ with an effective decay constant which is slightly less than 1 for $\mu > 0$; as would be anticipated this constant is larger than estimated in §6. The corresponding estimates for $\gamma(\mu, 0)$ are included in figure 22 (§9).

To effect the third analysis, we must recognize that backscattered waves ordinarily account for only a small fraction of the wave spectrum (Snyder (1974) roughly estimates this fraction at less than 2 % for most of his runs), and hence to the wave-sensor/wave-sensor matrix elements. Consequently it is not possible to resolve the backscattered spectrum from a wave-sensor array of the scope and precision employed in the Bight experiment. On the other hand, because the air-pressure signal generated by the backscattered spectrum is amplified relative to that generated by the main lobe of the spectrum, the backscattered spectrum contributes significantly to both wave-sensor/air-pressure-sensor elements and air-pressure-sensor/air-pressure-sensor elements.

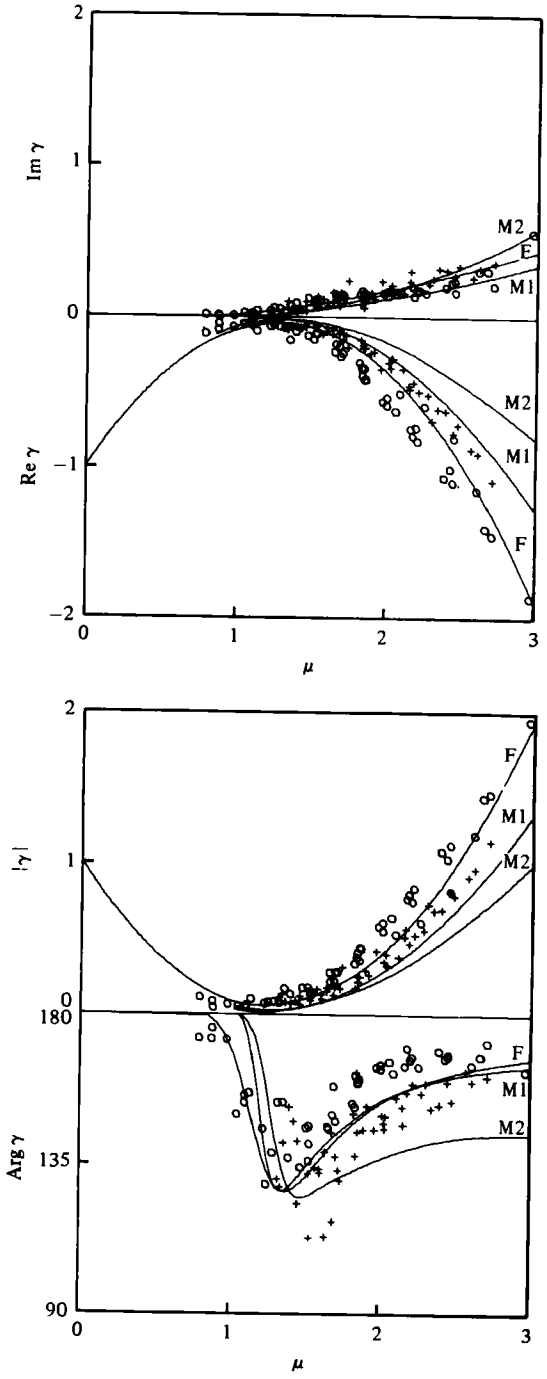

FIGURE 9. Test of general model: +, 1970 data (corrected for calibration error); ○, 1972 data (corrected for calibration error); F, best fit to 1970 data, general model (Snyder 1974); M1, Miles, $\Omega = 3 \times 10^{-3}$; M2, Miles, $\Omega = 2 \times 10^{-2}$.

Laguerre basis, no potential theory constraint

	S		
R	0	1	2
1	0·1247	0·1122	0·1058
2	0·0859	0·0853	0·0839
3	0·0846	0·0842	0·0910 (?)

Long–Miles basis, no potential theory constraint

	S		
R	0	1	2
1	0·1201	0·1091	0·1038
2	0·0861	0·0854	0·0842
3	0·0850	0·0828	0·0814

Laguerre basis, potential theory constraint

	S		
R	0	1	2
2	0·0961	0·0855	0·0848
3	0·0857	0·0852	0·0845

Long–Miles basis, potential theory constraint

	S		
R	0	1	2
2	0·0863	0·0857	0·0851
3	0·0863	0·0853	0·0859

TABLE 6. Proportional variances for linear analysis.

Laguerre basis, potential theory and uniqueness constraint, $Q = 2$

	S	
R	1	2
2	0·0855	0·0853
3	0·0854	0·0852

Long–Miles basis, potential theory and uniqueness constraint, $Q = 2$

	S	
R	1	2
2	0·0855	0·0856
3	0·0853	0·0853

TABLE 7. Proportional variance for bilinear analysis.

We note also that wave-sensor/air-pressure-sensor matrix elements depend explicitly on the product of E_{ζ^2} and γ, so that it is clear that we cannot expect to estimate both variables from these matrix elements alone. It will be necessary to include air-pressure-sensor/air-pressure-sensor elements (which depend on the triple product of E_{ζ^2}, γ and γ^*) in the analysis. It follows that in order to properly conclude our analysis

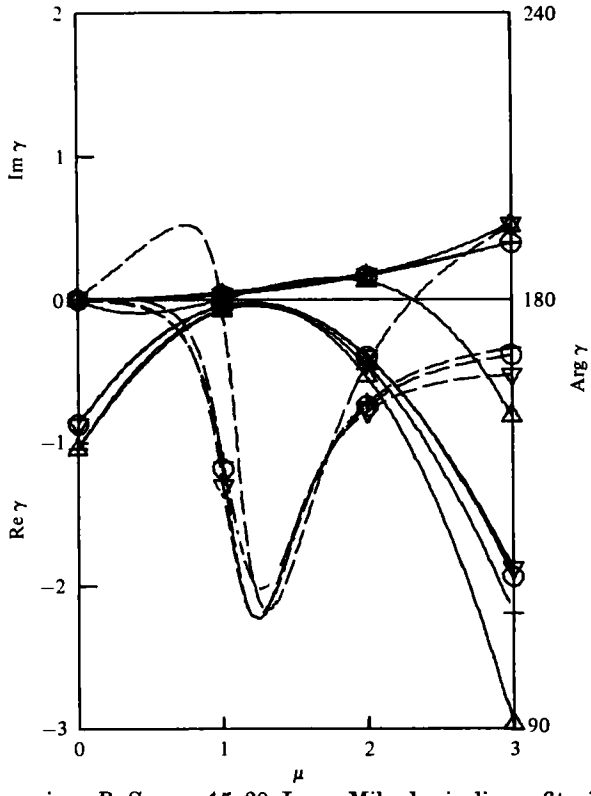

FIGURE 10. $\gamma(\mu, 0)$ for various R, S, runs 15–20. Long–Miles basis, linear fit with potential theory constraint. ○, $R = 2$, $S = 0$; +, $R = 2$, $S = 1$; ▽, $R = 3$, $S = 0$; △, $R = 3$, S = 1.

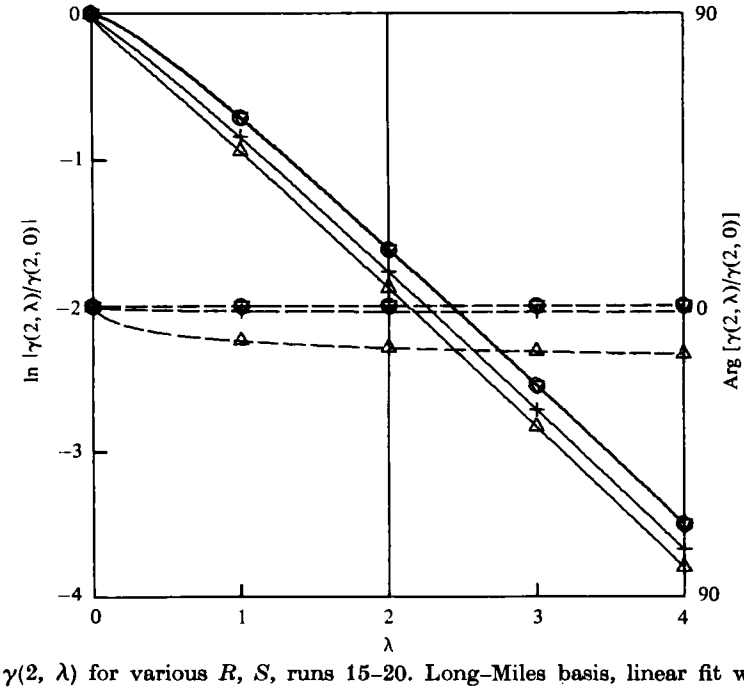

FIGURE 11. $\gamma(2, \lambda)$ for various R, S, runs 15–20. Long–Miles basis, linear fit with potential theory constraint. Phase lines are dashed. ○, $R = 2$, $S = 0$; +, $R = 2$, $S = 1$; ▽, $R = 3$, $S = 0$, △, $R = 3, S = 1$.

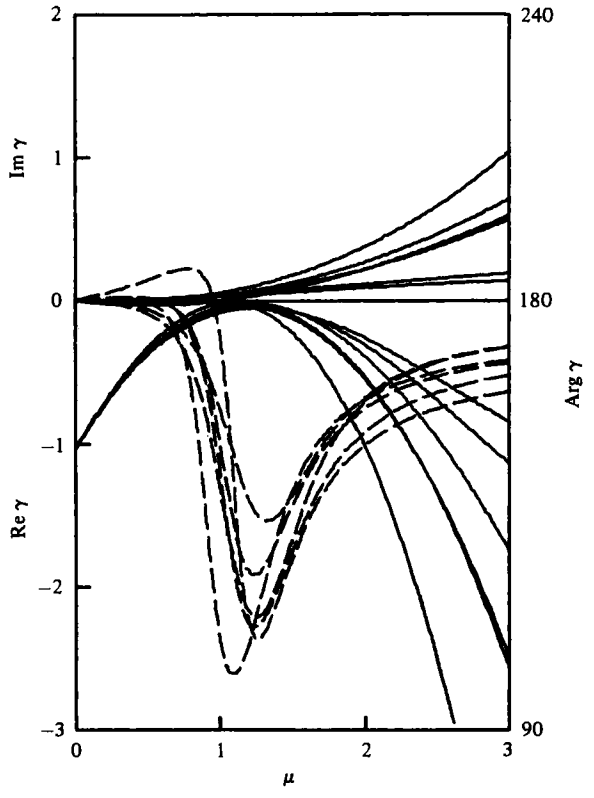

FIGURE 12. $\gamma(\mu, 0)$ for runs 15 to 20. Individual bilinear analysis, Long–Miles basis, with potential theory constraint, and $Q = 2$, $R = 1$ and $S = 1$.

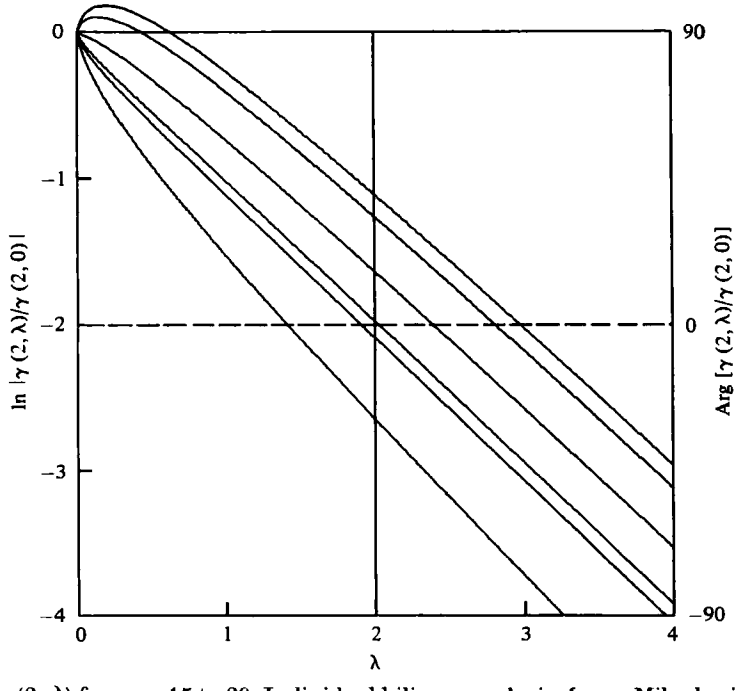

FIGURE 13. $\gamma(2, \lambda)$ for runs 15 to 20. Individual bilinear analysis, Long–Miles basis with potential theory constraint, and $Q = 2$, $R = 1$ and $S = 1$. Phase lines are dashed.

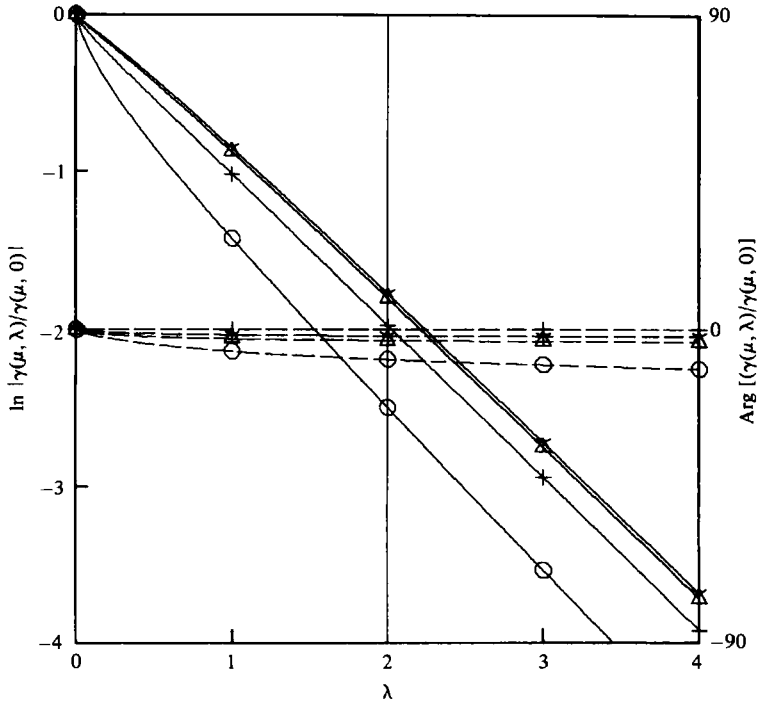

FIGURE 14. $\gamma(\mu, \lambda)$ for runs 15 to 20. Bulk linear analysis. Long–Miles basis, with potential theory constraint, and $R = 2$, $S = 1$. Phase lines are dashed. +, $\mu = 0$; ○, $\mu = 1$; Y, $\mu = 2$; △, $\mu = 3$.

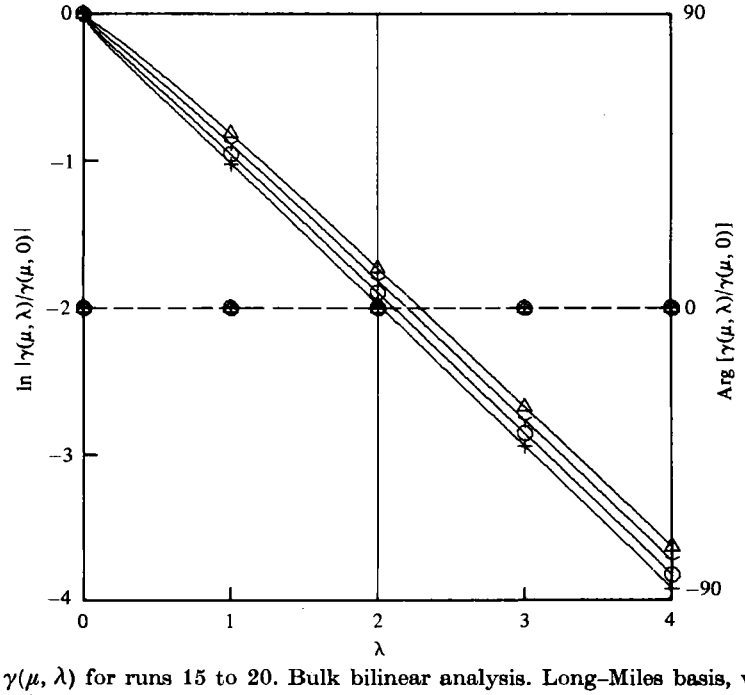

FIGURE 15. $\gamma(\mu, \lambda)$ for runs 15 to 20. Bulk bilinear analysis. Long–Miles basis, with potential theory constraint, and $Q = 2$, $R = 1$, and $S = 1$. Phase lines are dashed. +, $\mu = 0$; ○, $\mu = 1$; Y, $\mu = 2$; △, $\mu = 3$.

for γ, we will have to make allowance for turbulent air-pressure fluctuations which contribute to air-pressure-sensor/air-pressure-sensor elements. This latter complication is treated in some detail in the next section.

The simplest and most direct means of attempting the analysis is to: (1) assume some $\gamma(\mu, \lambda)$; (2) expand E_{ζ^2} in a basis set (linear or bilinear) allowing non-zero values for $|\theta| > \frac{1}{2}\pi$; (3) fix $E_{\zeta^2}(\omega, \theta)$ and $F_{Q^2}(\mathbf{k})$ by simultaneously fitting all matrix elements including air-pressure-sensor/air-pressure-sensor elements; (4) using the estimate of E_{ζ^2} from (3) re-estimate γ from wave-sensor/air-pressure-sensor elements; and (5) iterate steps (3) and (4) until E_{ζ^2}, F_{Q^2} and γ converge. We have tried this procedure and unfortunately find it to be divergent.

A second, somewhat more involved, procedure in which air-pressure-sensor/air-pressure-sensor elements are used directly to help estimate γ does converge. In this case we proceed initially as before, and then (3) fix E_{ζ^2} by simultaneously fitting wave-sensor/wave-sensor and wave-sensor/air-pressure-sensor elements; (4) subtract the corresponding wave-induced contribution from air-pressure-sensor/air-pressure-sensor elements and fix F_{Q^2} by fitting the residual elements; (5) subtract the corresponding turbulent contribution from air-pressure-sensor/air-pressure-sensor elements and re-estimate γ by simultaneously fitting the residual elements and wave-sensor/air-pressure-sensor elements; and (6) iterate steps (3), (4) and (5) until the procedure converges. The principal difficulty in implementing this procedure is that the air-pressure-sensor/air-pressure-sensor elements are quadratic functions of γ so that step (5) appears to involve a nonlinear fit. We circumvent the difficulty by treating one of the factors of γ as known (from the previous iteration), thus linearizing the fit.

To represent $E_{\zeta^2}(\omega, \theta)$, we augment the basis functions with an analogous set of functions defined to be zero for $|\theta| < \frac{1}{2}\pi$ and different from zero for $|\theta| > \frac{1}{2}\pi$. Using five of the former functions and three of the latter to represent the directional spectrum for run 14, we find that a joint analysis of runs 14 to 20 converges rapidly. The resulting estimate for E_{ζ^2} (run 14) is shown in figure 16. The estimate for γ is included in figure 22. For negative μ the phase is essentially zero, in agreement with the prediction of the Miles (1957) theory, but in disagreement with the previous analyses of both Dobson (1971) and Snyder (1974).

8. Analysis of turbulent fluctuations

The pressure spectra (figure 4) contains two regions of interest: a low-frequency region in which turbulent fluctuations dominate, and a central region in which surface-wave-induced fluctuations dominate (a third high-frequency region suggested by Snyder's (1974) data, in which turbulent fluctuations again dominate, is not so clearly evident in the present data). The boundaries of these regions depend on the wave spectrum, the wind speed, and the elevations of the pressure sensors. In the present case, the transition between the low-frequency region and the central region typically occurs somewhere between frequency bands 10 and 15 (0·25 Hz and 0·375 Hz). In this section, we will discuss our analysis of the turbulent fluctuations in both regions.

The turbulent component of atmospheric pressure in the atmospheric boundary layer has been the subject of previous field studies by Priestley (1965) and Elliott (1972*c*). Priestley investigated downwind and crosswind correlations of pressure along a land boundary; Elliott, downwind, crosswind, and vertical cross-spectra of

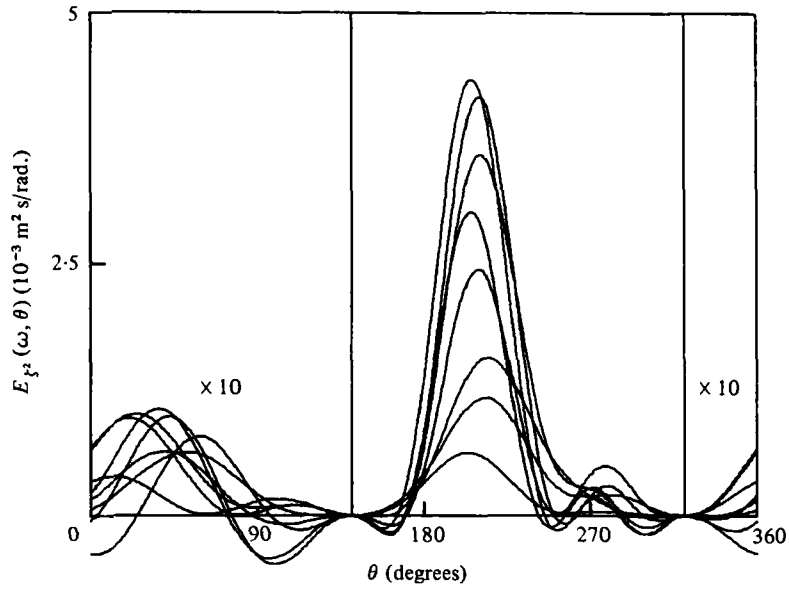

FIGURE 16. $E_{\zeta^2}(\omega, \theta)$ for run 14, bands 16 to 23. Backscatter analysis, linear fit. θ in degrees CCW from E, travel towards.

pressure within several metres of a land (and water) boundary. The Bight experiment yielded air-pressure/air-pressure cross-spectra between as many as seven instruments with spacings typically not precisely downwind, crosswind, nor vertical, and with a maximum downwind/crosswind spacing of approximately 10 m and a maximum vertical spacing of approximately 2 m.

Let the covariance $C_{Q^2}(\boldsymbol{\xi}, z_1, z_2, \tau)$ and the cross-spectrum $G_{Q^2}(\boldsymbol{\xi}, z_1, z_2, \omega)$ be defined as in §5. Note that C_{Q^2} is real and

$$C_{Q^2}(-\boldsymbol{\xi}, z_1, z_2, -\tau) = C_{Q^2}(\boldsymbol{\xi}, z_2, z_1, \tau).$$

It follows that

$$G_{Q^2}(\boldsymbol{\xi}, z_1, z_2, -\omega) = G^*_{Q^2}(\boldsymbol{\xi}, z_1, z_2, \omega)$$

and

$$G_{Q^2}(-\boldsymbol{\xi}, z_1, z_2, -\omega) = G_{Q^2}(\boldsymbol{\xi}, z_2, z_1, \omega).$$

Priestley suggests the extrapolation (his observations are confined to the ξ_1 and ξ_2 axes)

$$G_{Q^2}(\boldsymbol{\xi}, 0, 0, \omega) \simeq G_{Q^2}(\omega) \exp[-ik_1\xi_1] \exp[-\kappa_1|\xi_1| - \kappa_2|\xi_2|], \tag{12}$$

where ξ_1 and ξ_2 are the downwind and crosswind components of $\boldsymbol{\xi}$, κ_1 and κ_2 are given by the (MKS) power laws

$$\kappa_1 = 0{\cdot}32|k_1|^{1{\cdot}28}, \quad \kappa_2 = 1{\cdot}19\,\kappa_1^{0{\cdot}74},$$

where $k_1(\omega)$ is a downwind wavenumber given from the Taylor hypothesis of frozen turbulence by

$$k_1(\omega) = \frac{\omega}{U_{\mathbf{k}}}.$$

The advection speed $U_{\mathbf{k}}$ is approximated by

$$U_{\mathbf{k}} = U(\epsilon|k_1|^{-1}),$$

where $U(z)$ is the wind speed at elevation z, and ϵ is a constant of order 1 (Priestley found $\epsilon \simeq 1{\cdot}2$). Over several decades of ω, Priestley finds that the autospectrum G_{Q^2} is roughly proportional to ω^{-2}. This spectrum also varies roughly as U^4 (see Snyder & Cox 1966).

Elliott's downwind phases and crosswind coherences are reasonably consistent with, but his downwind coherences are significantly higher than, the values implied by (12). In agreement with Priestley, Elliott's autospectra also vary roughly as ω^{-2}. Elliott finds that the cross-spectrum $G_{Q^2}(0, z, z, \omega)$ is essentially independent of z. Vertical coherences between different elevations z_1, z_2, however, are comparable with crosswind coherences. These two observations suggest that close to the surface, i.e. for

$$\frac{\omega z_j}{U} \ll 2\pi, \quad j = 1, 2,$$

it may be appropriate to expand

$$G_{Q^2}(\boldsymbol{\xi}, z_1, z_2, \omega) = G_{Q^2}(\boldsymbol{\xi}, \omega) + (z_2 - z_1)\, G^{(\pm)}_{Q^2}(\boldsymbol{\xi}, \omega) + \ldots, \tag{13}$$

where the $+$ applies for $z_2 - z_1 > 0$, and the $-$ for $z_2 - z_1 < 0$ (a dual expansion is suggested to allow for a discontinuity in slope for $z_2 = z_1$, such as would be implied by a dependence like $e^{-\kappa|z_2 - z_1|}$). We have

$$G_{Q^2}(\boldsymbol{\xi}, -\omega) = G^*_{Q^2}(\boldsymbol{\xi}, \omega)$$

with corresponding relations for $G^{(\pm)}_{Q^2}(\boldsymbol{\xi}, \omega)$.

In what follows, we will provide an interpretation of the results of Priestley and Elliott based on a modified 'frozen' turbulence model, and will use this model to estimate for the present data an 'intrinsic' turbulent pressure spectrum $F_{Q^2}(\mathbf{k})$ arising from the first term on the right-hand side of (13). The vertical inhomogeneity of the pressure field and the measurable loss of coherence in the vertical greatly complicate the model. Because the vertical spacing of instruments for the Bight experiment is small compared with their crosswind spacing we have chosen to neglect these complications by truncating expansion (13) after the first term. Limited computations including a second term in the subsequent fits indicate that the complications do not appreciably alter results for the present data. Let

$$F_{Q^2}(\mathbf{k}, z_1, z_2, \omega) \equiv \frac{2}{(2\pi)^3} \int_{-\infty}^{\infty} d^2\xi \int_{-\infty}^{\infty} d\tau\, C_{Q^2}\, e^{-i(\mathbf{k}\cdot\boldsymbol{\xi} - \omega\tau)}$$

be the three-dimensional cross-spectrum of turbulent pressure. We have

$$F_{Q^2}(-\mathbf{k}, z_1, z_2, -\omega) = F^*_{Q^2}(\mathbf{k}, z_1, z_2, \omega),$$

$$F_{Q^2}(\mathbf{k}, z_2, z_1, \omega) = F^*_{Q^2}(\mathbf{k}, z_1, z_2, \omega)$$

and

$$G_{Q^2}(\boldsymbol{\xi}, z_1, z_2, \omega) = \int_{-\infty}^{\infty} d^2k\, F^*_{Q^2}\, e^{-i\mathbf{k}\cdot\boldsymbol{\xi}}.$$

From (13) we anticipate that

$$F_{Q^2}(\mathbf{k}, z_1, z_2, \omega) = F_{Q^2}(\mathbf{k}, \omega) + (z_2 - z_1)\, F^{(\pm)}_{Q^2}(\mathbf{k}, \omega) + \ldots.$$

It follows that

$$F_{Q^2}(-\mathbf{k}, -\omega) = F^*_{Q^2}(\mathbf{k}, \omega) = F_{Q^2}(\mathbf{k}, \omega) > 0$$

and

$$G_{Q^2}(\boldsymbol{\xi}, \omega) = \int_{-\infty}^{\infty} d^2k\, F_{Q^2}(\mathbf{k}, \omega)\, e^{-i\mathbf{k}.\boldsymbol{\xi}}$$

with corresponding relations for $F^{(\pm)}_{Q^2}(\mathbf{k}, \omega)$.

The frozen turbulence hypothesis imagines that the time scale of the adjustment to inhomogeneities in the flow is sufficiently long compared with the time scale with which these inhomogeneities are advected that the inhomogeneities appear frozen in the flow. Thus for every $\mathbf{k}$ we can find a reference frame (moving with the advection velocity $\mathbf{U}_{\mathbf{k}}$) in which $F_{Q^2}(\mathbf{k}, \omega)$ is concentrated at $\omega = 0$. It follows that in the fixed frame F_{Q^2} is approximated by

$$F_{Q^2}(\mathbf{k}, \omega) = F_{Q^2}(\mathbf{k})\, \delta(\omega - \mathbf{k}.\mathbf{U}_{\mathbf{k}}), \tag{14}$$

where the 'intrinsic' spectrum $F_{Q^2}(\mathbf{k})$ is a positive even function of $\mathbf{k}$

$$F_{Q^2}(-\mathbf{k}) = F^*_{Q^2}(\mathbf{k}) = F_{Q^2}(\mathbf{k}) > 0$$

assuming $\mathbf{U}_{-\mathbf{k}} = \mathbf{U}_{\mathbf{k}}$.

It also follows that

$$G_{Q^2}(\boldsymbol{\xi}, \omega) = \int_{-\infty}^{\infty} d^2k\, F_{Q^2}(\mathbf{k})\, \delta(\omega - \mathbf{k}.\mathbf{U}_{\mathbf{k}})\, e^{-i\mathbf{k}.\boldsymbol{\xi}}.$$

For simplicity we assume

$$\mathbf{U}_{\mathbf{k}} = \mathbf{U}(\epsilon |k_1|^{-1}).$$

Then

$$\mathbf{k}.\mathbf{U}_{\mathbf{k}} = k_1\, U(\epsilon |k_1|^{-1})$$

which suggests the change of variables

$$(k_1, k_2) \to (\omega_1, k_2),$$

where

$$\omega_1(k_1) \equiv k_1\, U(\epsilon |k_1|^{-1}).$$

Thus

$$G_{Q^2}(\boldsymbol{\xi}, \omega) = J(\omega)\, e^{-ik_1(\omega)\xi_1} \int_{-\infty}^{\infty} dk_2\, F_{Q^2}[k_1(\omega), k_2]\, e^{-ik_2\xi_2}, \tag{15}$$

where $k_1(\omega_1)$ is the inverse of $\omega_1(k_1)$ and $J(\omega_1)$ is the Jacobian

$$J(\omega_1) \equiv \frac{\partial[k_1(\omega_1), k_2]}{\partial(\omega_1, k_2)} = \frac{d}{d\omega_1} k_1(\omega_1). \tag{16}$$

For a logarithmic wind profile, $J(\omega_1)$ is roughly constant over a broad range of ω_1, and correspondingly k_1 is roughly linear in ω_1.

It is of interest to examine the integral (15) for the special case of an isotropic power law

$$F_{Q^2}(\mathbf{k}) = F_{Q^2} k^{-\nu}.$$

We have

$$G_{Q^2}(\boldsymbol{\xi}, \omega) = JF_{Q^2} k^{-\nu+1}\, e^{-ik_1\xi_1} \int_{-\infty}^{\infty} \mathrm{d}\sigma (1+\sigma^2)^{-\frac{1}{2}\nu}\, e^{-i\sigma k_1 \xi_2}. \tag{17}$$

For $\nu = 2$

$$G_{Q^2} = \pi J F_{Q^2} k_1^{-1}\, e^{-ik_1\xi_1} e^{-|k_1\xi_2|},$$

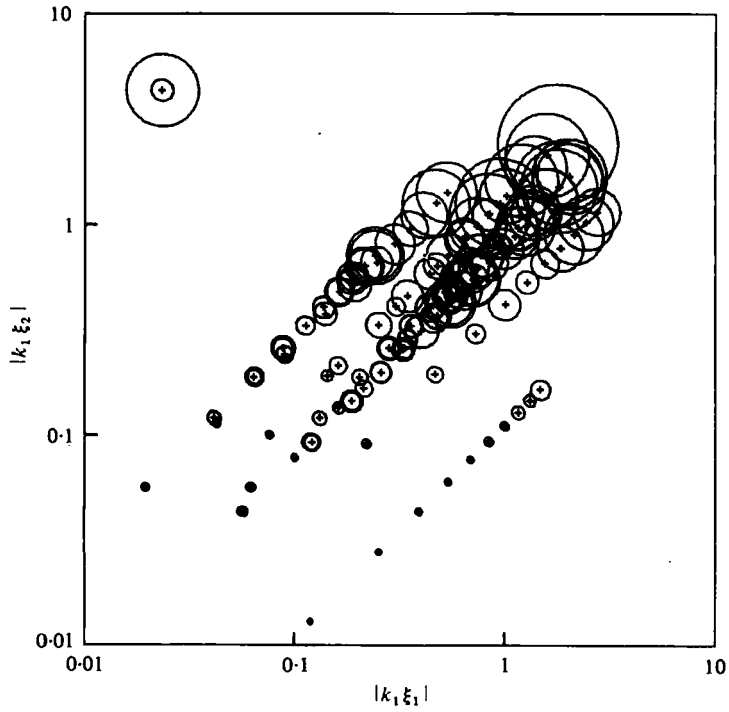

FIGURE 17. Coherence plot for run 16, low frequency (turbulent) bands. ξ is displacement of air-pressure sensor pair. Diameter of circles is proportional to the negative logarithm of the squared coherence. Circles to left of plot define the scale for squared coherence of 0·5 and 0·1.

while for $\nu = 3$

$$G_{Q^2}(\xi, \omega) = JF_{Q^2} k_1^{-2} e^{-ik_1\xi_1} |k_1\xi_2| K_1(|k_1\xi_2|),$$

where $K_1(z)$ is a modified Bessel function of the third kind. Note that for small z, $zK_1(z) \to 1$, while for large z, $zK_1(z) \to (\frac{1}{2}\pi z)^{\frac{1}{2}} e^{-z}$.

In each case, the phase is given by $-k_1\xi_1$, the coherence is a function of $k_1\xi_2$ (and is therefore independent of ξ_1), and the autospectrum goes roughly as $\omega^{-\nu+1}$. For $\nu = 2$, G_{Q^2} is of the form (12) with $\kappa_1 = 0$ and $\kappa_2 = |k_1|$. We further note that Priestley's power laws for κ_1 and κ_2 may be combined to give (MKS)

$$\kappa_2 = 0{\cdot}52|k_1|^{0{\cdot}95},$$

roughly half the $\nu = 2$ result. For $\nu = 3$ the autospectrum goes roughly as ω^{-2}, in agreement with both Priestley and Elliott.

Thus a simple frozen turbulence model is, with varying assumptions, able to reproduce certain features of previous observations of turbulent pressure above a land boundary. The model does not reproduce the loss of coherence due to vertical or downwind separation. The first failing, which results from the neglect of terms beyond the constant term in (13), is in principle reparable by extending the theory to higher order. The second failing is intrinsic to the concept of frozen turbulence: if the turbulence is truly frozen, two instruments downwind of one another should see an essentially identical signal displaced in time; the resulting coherence should be unity.

Figure 17 shows the coherence for run 16 for all instrument pairs, frequency bands

1 to 10, as a function of $k_1\xi_1$ and $k_1\xi_2$. This plot is typical of the higher wind-speed runs. The figure clearly suggests that to some level of approximation the coherence is primarily a function of $k_1\xi_2$, in agreement with the frozen turbulence hypothesis, and in disagreement with the extrapolation (12). How then do we account for loss of coherence in the downwind direction observed by both Priestley and Elliott?

It is clear that some of this loss of coherence must result from the inadequacies of the frozen turbulence hypothesis. A broadening of the delta function in (14) would undoubtedly lead to a more realistic (but less readily integrable) model for G_{Q^2}, with some downwind loss of coherence. Presumably this loss of coherence would be of the same order as that observed by Willmarth & Wooldridge (1962) in their wind tunnel studies of turbulent wall pressure fluctuations. As is evident from figure 20, however, the downwind loss of coherence observed by both Priestley and Elliott is significantly larger than that observed by Willmarth & Wooldridge.

We suggest that a more significant source of downwind ($|\xi_2| \ll |\xi_1|$) loss of coherence in a field situation lies in the natural variability of wind direction and the associated variability in ξ_1 and ξ_2. Two instruments nominally downwind of one another are only rarely precisely downwind of one another. Because the crosswind coherence drops off fairly rapidly near zero crosswind displacement, a small variation in wind direction will result in a measurable loss of coherence for such instruments. We may estimate this loss of coherence for the isotropic case $\nu = 2$ by noting that for $\overline{\xi_2} = 0$ and $\theta \equiv \mathrm{Arg}(\boldsymbol{\xi})$ small,

$$\overline{\exp[-|k_1\xi_2|]} \simeq \exp[-\overline{|\theta|}\,|k_1\xi|],$$

where the overbar denotes a time average. This result is consistent with (12) (for $\xi_2 = 0$) if

$$\kappa_1 \simeq \overline{|\theta|}\,|k_1|.$$

Away from the ξ_1 axis the effect of wind direction variability on the coherence may likewise be assessed by taking a time average of the frozen turbulence result (taking z_1 and z_2 as functions of time). In this case, however, the effect is considerably smaller; the resulting loss of coherence is comparable with the unaveraged loss.

Figures 18, 19 and 20 show the results of first-order polynomial fits in ξ_1 and ξ_2, to $\mathrm{Arg}\,G_{Q^2}(\boldsymbol{\xi},\omega)$ and $\ln\mathrm{Coh}\,G_{Q^2}(\boldsymbol{\xi},\omega)$ in each band of all runs for which $U_5 > 3\,\mathrm{m\,s^{-1}}$. Figure 18 shows the results of the fit

$$\mathrm{Arg}\,G_{Q^2}(\boldsymbol{\xi},\omega) \simeq -k_1\xi_1.$$

The best fit k_1 is plotted against $k_1(\omega)$ computed for $\epsilon = 1{\cdot}5$. Shown also are points from Elliott's figure 33(*b*) and the prediction of the frozen turbulence model. Figure 19 shows the results of the fit

$$\ln\mathrm{Coh}\,G_{Q^2}(\boldsymbol{\xi},\omega) \simeq -\kappa_2|\xi_2|.$$

The best fit κ_2 is plotted against $|k_1(\omega)|$. Shown also are points from Elliott's figure 32, Priestley's power law, the prediction of an isotropic power law for $\nu = 2$ and the predictions of an isotropic power law for $\nu = 3$ with $|\xi_2| = 1\,\mathrm{m}$ and $|\xi_2| = 10\,\mathrm{m}$ respectively. Finally, to give some idea of the scale of the downwind loss of coherence, figure 20 shows the results of the fit

$$\ln\mathrm{Coh}\,G_{Q^2}(\boldsymbol{\xi}_1,\omega) \simeq -\kappa_1|\xi_1| - \kappa_2|\xi_2|.$$

The best fit κ_1 is plotted against $k_1(\omega)$; shown also are points from Elliott's figure 33(*a*),

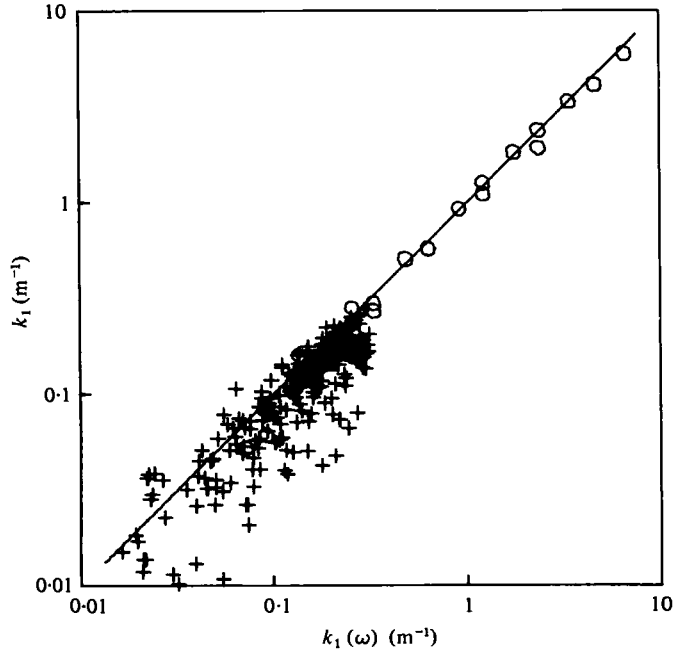

FIGURE 18. Downwind wavenumber. k_1 from best fit to phase of air-pressure/air-pressure matrix elements, $k_1(\omega)$ computed for $\epsilon = 1{\cdot}5$. +, this experiment; ○, Elliott (1972*c*); —, $k_1 = k_1(\omega)$.

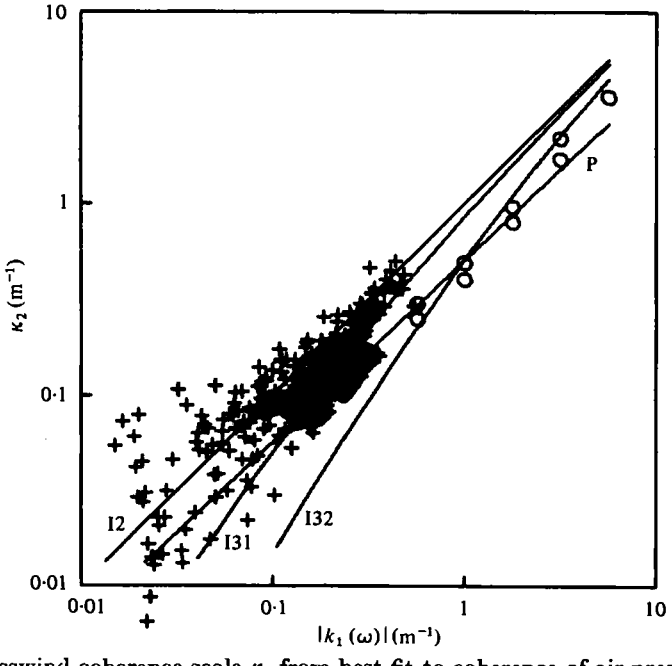

FIGURE 19. Crosswind coherence scale κ_2 from best fit to coherence of air-pressure/air-pressure matrix elements. $k_1(\omega)$ computed for $\epsilon = 1{\cdot}5$. +, this experiment; ○, Elliott (1972*c*); P, Priestley (1965); I2, $\nu = 2$ power law; I31, $\nu = 3$ power law, $|\xi_2| = 1$ m; I32, $\nu = 3$ power law, $|\xi_2| = 10$ m.

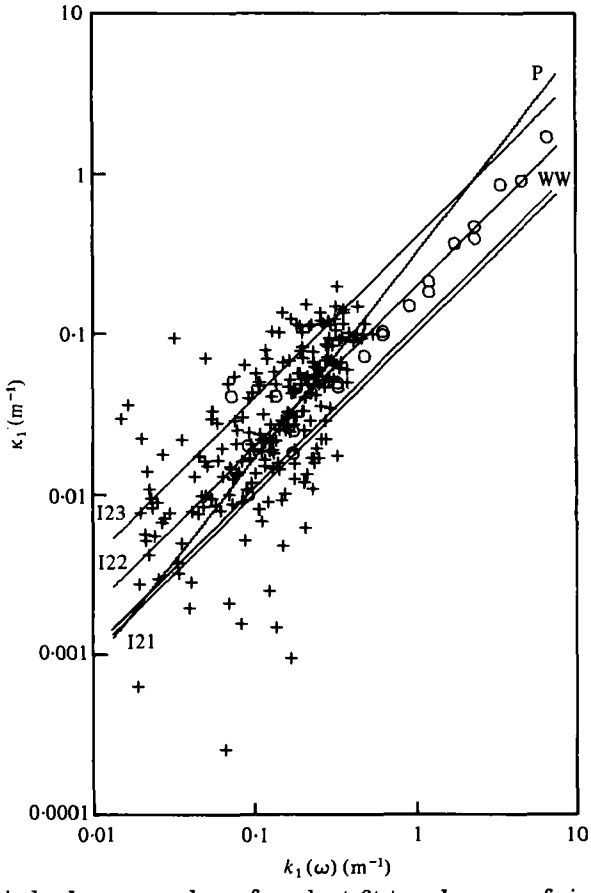

FIGURE 20. Downwind coherence scale. κ_1 from best fit to coherence of air-pressure/air-pressure matrix elements. $k_1(\omega)$ computed for $\epsilon = 1{\cdot}5$. +, this experiment; ○, Elliott (1972*c*); P, Priestley (1965); WW, Willmarth & Wooldridge (1962); I21, $\nu = 2$ power law, $|\overline{\theta}| = 0{\cdot}1$; I22, $\nu = 2$ power law, $|\overline{\theta}| = 0{\cdot}2$; I23, $\nu = 2$ power law, $|\overline{\theta}| = 0{\cdot}4$.

Priestley's power law, the predictions of a modified frozen turbulence model for $\nu = 0$, $|\overline{\theta}| = 0{\cdot}1, 0{\cdot}2$, and $0{\cdot}4$, and the results of Willmarth & Wooldridge's wind-tunnel study.

These figures suggest that the present data are on average consistent with an intrinsic turbulent pressure spectrum which goes as k^{-2}, with $|\overline{\theta}|$ approximately $0{\cdot}1$ to $0{\cdot}4$. Priestley and Elliott appear to favour a spectrum which goes more like k^{-3}, consistent with an ω^{-2} power law for G_{Q^2}; note that at the lower frequencies the slope of both spectra is reduced. If our interpretation of downwind loss of coherence is correct, the variability in wind direction was greater for Priestley than for Elliott. Willmarth & Wooldridge's downwind loss of coherence is equivalent to that predicted by our model for $\nu = 2$ and $|\overline{\theta}| = 0{\cdot}11$.

Further analysis of the turbulent component of the air pressure fluctuations has been directed toward estimating $F_{Q^2}(\mathbf{k})$ via a least squares fit to air pressure/air pressure cross-spectral elements. To effect this analysis we expand

$$F_{Q^2}(\mathbf{k}) = \chi\left(\frac{k_2}{k_1}\right)\sum_n^N {}_nF_{Q^2}(k_1)\,\psi_n\left(\frac{k_2}{k_1}\right), \quad \text{for linear analysis,}$$

or

$$F_{Q^2}(\mathbf{k}) = \chi\left(\frac{k_2}{k_1}\right)\left(\sum_n {}_nF_{Q^2}(k_1)\,\psi_n\left(\frac{k_2}{k_1}\right)\right)^2, \quad \text{for bilinear analysis.}$$

The prefix χ and basis set ψ_n are defined by

$$\chi(\sigma) \equiv \frac{e^{-|\sigma|}(1+|\sigma|)}{(1+\sigma^2)^r} \quad \text{with} \quad r = \tfrac{1}{2}, 1,$$

and

$$\psi_n(\sigma) \equiv \sigma^{s(n-1)} \quad \text{with} \quad s = 1, 2.$$

For $N = 1, r = \frac{1}{2}$, and $F_{Q^2} \sim k_1^{-2}$ (linear analysis) this superposition approximates the simple relation

$$F_{Q^2}(\mathbf{k}) \sim k^{-2}$$

over the limited range $|k_2/k_1| \leqslant 2$.

An acceptable representation of this power law (or of a k^{-3} law) over the broader range $|k_2/k_1| \leqslant 10$ can be constructed for $N = 5$ and $s = 2$ using either choice for r. The simpler choice

$$\chi(\sigma) = e^{-\sigma^2}$$

related to the Hermite polynomials was not used because the spread towards larger σ goes as $n^{\frac{1}{2}}$ rather than n; consequently a larger number of terms are required to produce an adequate representation over a given range.

To estimate $F_{Q^2}(\mathbf{k})$ in the turbulent bands we minimize the variance (linear analysis)

$$V(\omega) \equiv \sum_{jl} |G_{jl}(\omega) - \sum_n^N K_{jln}(\omega)\,{}_nF_{Q^2}[k_1(\omega)]|^2$$

or the variance (bilinear analysis)

$$V(\omega) = \sum_{jl} |G_{jl}(\omega) - \sum_m^M \sum_n^N K_{jlmn}(\omega)\,{}_mF_{Q^2}[k_1(\omega)]\,{}_nF_{Q^2}[k_1(\omega)]|$$

with respect to the real coefficients ${}_nF_{Q^2}[k_1(\omega)]$ (the outer sum runs over air-pressure/air-pressure matrix elements). The coefficients K_{jln} and K_{jlmn} are given by

$$K_{jln}(\omega) \equiv J(\omega)\,k_1(\omega)\exp[-ik_1(\omega)\,\xi_{jl1}]\int_{-\infty}^{\infty} d\sigma\,\chi(\sigma)\,\psi_n(\sigma)\exp[-i\sigma k_1(\omega)\xi_{jl2}]$$

and

$$K_{jlmn}(\omega) \equiv J(\omega)k_1(\omega)\exp[-ik_1(\omega)\xi_{jl1}]\int_{-\infty}^{\infty} d\sigma\,\chi(\sigma)\psi_m(\sigma)\psi_n(\sigma)\exp[-i\sigma k_1(\omega)\xi_{jl2}].$$

In the wave bands we minimize the variance (linear analysis)

$$V(\omega) \equiv \sum_{jl} M_{jl}^2 |G_{jl}(\omega) - \sum_m^M H_{jlm}(\omega)\,{}_mE_{\zeta^2}(\omega) - \epsilon_{jl}\sum_n^N K_{jln}(\omega)\,{}_nF_{Q^2}[k_1(\omega)]|^2$$

with respect to both the ${}_mE_{\zeta^2}(\omega)$ and ${}_nF_{Q^2}[k_1(\omega)]$. The sum runs over all cross-spectral elements, with $\epsilon_{jl} = 1$ for air-pressure/air-pressure elements and $\epsilon_{jl} = 0$, otherwise. The computation assumes that $\mathbf{D}(\omega, \theta)$ and $\gamma(\mu, \lambda)$ [necessary to form the $H_{jln}(\omega)$] are already known.

The run 16, $r = 1, s = 2, N = 2$, estimate for F_{Q^2} is displayed in figure 21. Each cut

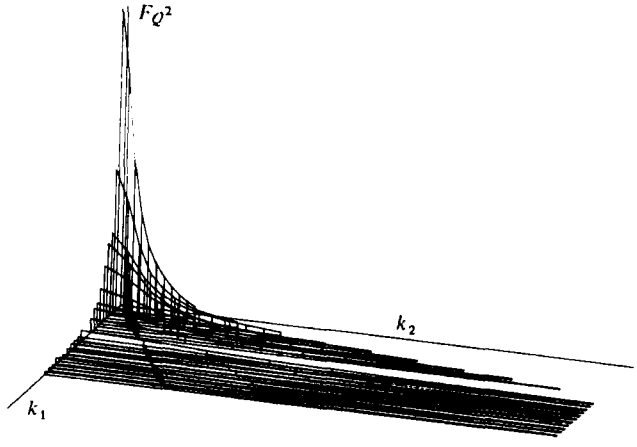

FIGURE 21. Intrinsic turbulent pressure spectrum F_{Q^2} for run 16. F_Q axis extends to 0·1 Pa² m²; k_1 axis extends to 1 m⁻¹.

Run	ν†	a_{01}	$e^{2a_{01}}$
1	2·09/2·19	0·074	1·16
4	2·52/2·64	−0·344	0·50
5	2·59/2·73	−0·221	0·64
6	2·59/2·74	−0·565	0·32
7	1·35/2·55	−0·287	0·56
14	1·79/1·85	0·145	1·34
15	1·82/1·77	−0·008	0·98
16	1·88/1·78	−0·029	0·94
17	1·85/1·67	−0·106	0·81
18	1·88/1·68	−0·58	0·89
19	1·98/1·60	0·231	1·59
20	1·99/1·72	−0·127	0·78
31	1·85/1·72	0·132	0·77
32	1·54/2·22	0·073	1·16
34	2·65/2·70	0·396	2·21

† First entry from best fit to $F_{Q^2}(\mathbf{k})$; second entry from slope of low-frequency tail of $G_{P^2}(\omega)$.

TABLE 8. Parametrization of 'intrinsic' turbulent pressure spectrum. Fit to low-frequency bands.

parallel to the k_1 axis results from the analysis within a given frequency band. The cuts are in two groups, corresponding to bands 1 to 10 (turbulent bands) and bands 13 to 23 (wave bands). Only a single quadrant of F_{Q^2} is shown since the estimate has been constrained to be an even function of both variables.

The horizontal isotropy of the turbulent pressure field was investigated by fitting the resulting estimates for $F_{Q^2}(\mathbf{k})$, bands 1 to 10, from various runs for $(k_2/k_1) \leqslant 5$ to a representation of the form

$$F_{Q^2}(\mathbf{k}) = k^{-\nu} \exp\left[a_{00} + a_{01} \cos 2\theta\right].$$

The results of this fit (taking the natural logarithm of both sides makes the computation linear) are summarized in table 8. For the most part the spectra are reasonably isotropic, but significant anisotropy of both signs is not uncommon. Note that, as

would be anticipated from equation (17), the best-fit values for ν are reasonably consistent with values estimated from the slope of the low-frequency tail of the air-pressure autospectra.

9. Implications for wave growth and momentum transfer

Assuming that the atmospheric interaction is controlled by the atmospheric pressure field, the linear part of source function A_{ζ^2} appearing in the deep-water (zero-drift) radiation-balance equation is given by

$$A_{\zeta^2} = \frac{2\pi}{\rho^2 g^4}\omega^5 F_{Q^2}[\mathbf{k}(\omega,\theta), -\omega] + s\omega \operatorname{Im}[\gamma] E_{\zeta^2}(\omega,\theta),$$

where the turbulent spectrum F_{Q^2} and the dimensionless wave-induced pressure ratio γ are evaluated at the mean surface.

Previous estimates of the turbulent contribution to A_{ζ^2} have been based primarily on Priestley's extrapolation (12), extended to higher wind speeds with a U^4 power law (see Snyder & Cox 1966). The resulting contribution is unimportant except perhaps at low frequency and large fetch (Ross & Cardone 1978). The analysis of §8 suggests that in fact such estimates are incorrect. It is our contention that Priestley's extrapolation (12) applies only along the ξ_1 and ξ_2 axes and only under conditions of strong variability in wind direction. Away from these axes, relation (12) overpredicts the loss of coherence.

On the other hand, the 'frozen turbulence' model of §8 gives a non-vanishing contribution to A only for wave components satisfying the dispersion relation

$$\omega = \mathbf{k}(\omega,\theta).\mathbf{U}_{\mathbf{k}}.$$

For such components this contribution is infinite. Clearly we cannot use a 'frozen turbulence' model to estimate the turbulent contribution, either. What is required is a softening of the delta function in (14). One way to accomplish this is to replace the delta function with a Gaussian, and fix the spread parameter as part of the least squares analysis of air-pressure/air-pressure matrix elements (a nonlinear computation). We have not attempted this and do not know if it would be successful. We anticipate that the computation would require a large body of relatively clean data from sensors placed at the same elevation; otherwise the loss of coherence in the vertical would have to be treated simultaneously. Our guess is that the resulting spread would be an order of magnitude smaller than implied by (12) and therefore that the turbulent contribution to A_{ζ^2} would be significantly larger or smaller than presently supposed, depending on how close to resonance the particular component is.

The wave-induced contribution to A_{ζ^2} is defined by the imaginary part of the dimensionless air pressure ratio γ evaluated at the mean surface. A summary of various estimates of $\gamma(\mu, 0)$ resulting from the analysis of §§6 and 7 is presented in figure 22. Also included in the figure are corrected γ curves computed from the data sets of Dobson (1971), Elliott (1972*b*), and Snyder (1974), and the simple relation

$$\operatorname{Im}\gamma \begin{cases} = 0{\cdot}2(\mu - 1), & \mu \geqslant 1, \\ = 0, & \mu < 1. \end{cases} \tag{18}$$

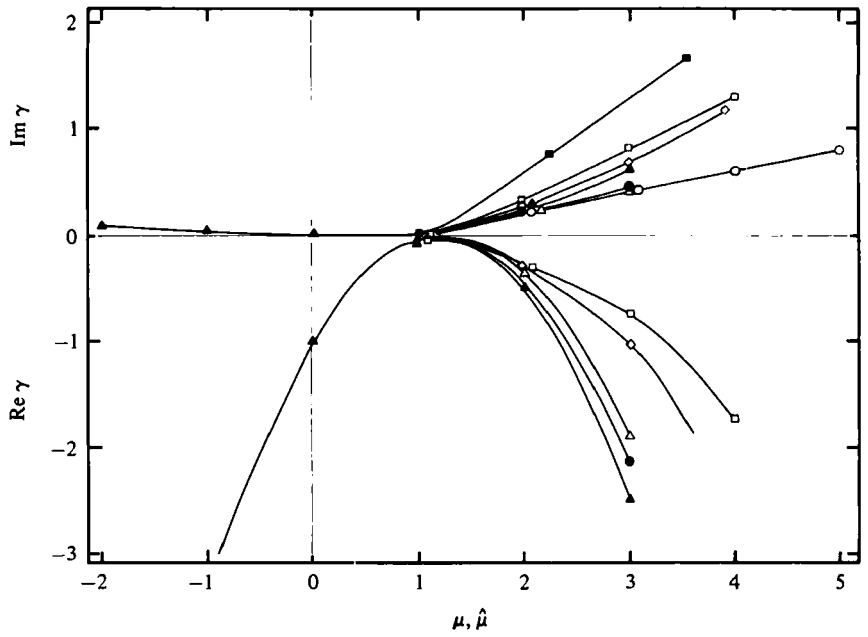

FIGURE 22. $\gamma(\mu, 0)$ summary. Solid curves above abscissa are for Im γ. Solid curves below abscissa are for Re γ. ■, Dobson (1971); □, Elliott (1972); ◇, simplified (BIO) analysis runs 15 to 20, 4, 7, 33, 34; △, Snyder (1974) corrected for calibration error; ●, runs 15 to 20, general model, bilinear Long–Miles basis, Q, R, S = 2, 1, 1; ▲, runs 14 to 20, general model, linear Laguerre basis, R, S = 3, 0; ○, Im γ = 0·2 $(\mu - 1)$.

In each case the data sets have been reworked using the same techniques employed in the present analysis. Both Dobson's and Elliott's μ values have been rescaled to $\hat{\mu} = (8/3\pi)\mu$ to allow for a wave directional spread, as in §6. In addition Dobson's $\hat{\mu}$ values were modified to allow for the presence of significant upwind drift currents in some of the runs (see Dobson 1971, table 1), Elliott's γ estimates have been computed from the original data set and included, and Snyder's curves have been corrected for the calibration error noted in §2.

The corrected Elliott (1972*b*) and Snyder (1974) Im γ curves are in good agreement with the BOA data as described by the two model fits shown; the differences between the model fits and the simplified analysis are within experimental error. Dobson's corrected Im γ estimates remain a factor of 2 to 3 greater than any of the other estimates: a factor of 2 greater than Elliott (1972*b*) and of 3 above Snyder (1974). The reasons for the high growth rates estimated by Dobson remain unclear. For a given μ value and at comparable fetches his wave-pressure quadrature spectra were roughly the same as for the present data set, but his wave spectral estimates were smaller. On the other hand, scaling Dobson's wave spectra against the JONSWAP model (Hasselmann *et al.* 1973) indicates them to be on the low side, but within the scatter of the JONSWAP data.

The Re γ estimates show a wider disparity between the simplified and general models than do those of Im γ. The most striking difference is between the separate analyses by the BIO and Nova groups of the same data set; each analysis agrees well with earlier data analysed the same way.

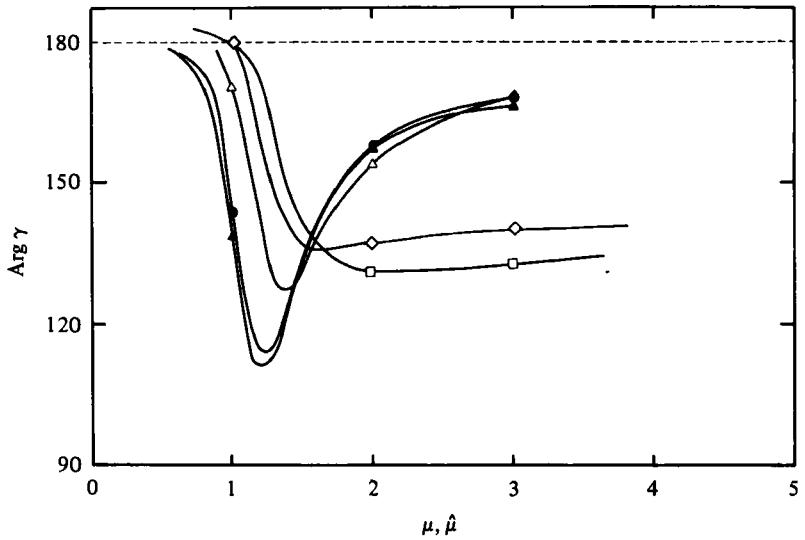

FIGURE 23. Phase (Arg γ) summary. Symbols as for figure 22.

The differences between the simplified and general model results for the wave-pressure phase difference Arg γ (figure 23) are obvious, and although phase measurements are notorious for noise sensitivity and scatter, the differences shown are well beyond experimental error bounds, particularly for $\mu > 2$.

We consider below some possible reasons for the observed differences; we consider first differences in the analysis techniques and, in the case of earlier measurements, in the sites, and then differences in instrumentation.

(*a*) *μ scaling*

The parameter μ is given by

$$\mu \equiv \frac{\mathbf{k}.\mathbf{U}}{\omega} = \frac{k(\mathbf{D},\theta)\, U \cos(\theta - \Theta)}{\omega}.$$

For given (ω, θ), μ is a function of the wind azimuth Θ and the effective drift $\mathbf{D}(\omega, \theta)$. Generally μ is a maximum if the wind azimuth and wave azimuth coincide ($\theta = \Theta$) and the drift vanishes (discounting upwave drift). If $\theta - \Theta \neq 0$, $\cos(\theta - \Theta) < 1$; if $\mathbf{k}.\mathbf{D} > 0$, k is reduced; in either case μ is lowered. Both effects are included in the analyses of Snyder (1974) and of §7. The analysis of §6 ignores the second effect but makes partial allowance for the first [by assuming $\cos^2(\theta - \phi)$ directional spreading]. This allowance is only partial because in the μ computation the principal wave azimuth ϕ is assumed to coincide with the wind azimuth Θ. As shown in table 4 a lack of coincidence between these azimuths is significant only for difference angles in excess of 20°. The Bight of Abaco site has a rather unsymmetrical fetch distribution, so that in fact such differences are common, particularly at the lower frequencies. Even at frequencies somewhat in excess of the peak frequency, such differences are not uncommon (see figure 8). Section 6 makes a correction of about 15 % to the scale of μ; probably this correction should be on average roughly 5 % greater.

The downwave component of the effective drift, as determined by the directional

spectrum analysis of §7, is typically an increasing function of frequency rising to a value of 0·1 to 0·2 m s^{-1} at frequencies approaching 1 Hz. At higher frequencies this drift is probably still larger. The resulting proportional reduction in k and μ is given by the ratio between the drift and the phase speed (the parameter ν of §5); for the higher frequencies analysed this ratio is typically about 10%.

An additional reduction of 15% in the §6 values for μ (giving a total reduction of 30%) would bring the figure 8 estimates for Re γ much closer to those resulting from the analysis of §7.

In fact the considerations of §5 suggest that the parameter μ is not entirely appropriate to the analysis. An invariant form of this parameter is

$$\frac{\mu-\nu}{1-\nu} = \mu + (\mu-1)\nu + \ldots.$$

For $\mu \geqslant 1$, the implied correction opposes the scale changes discussed above. At $\mu = 1$ the correction vanishes; at $\mu = 2$ it is one-half the size of the previous drift correction; at $\mu = 3$, two-thirds the size, etc. The principal effect of applying this correction would be to elevate μ for Snyder (1974) and §7 and to lessen the drift-induced reduction in μ for Elliott (1972*b*) and §6.

Note that while the above corrections would improve the agreement in the estimates for Re γ, they would adversely affect the present agreement between the corresponding estimates for Im γ. The Im γ estimates are in remarkably good agreement, with the exception of Dobson's (1971) 'corrected' curve.

(*b*) *Incomplete parametrization of the dynamics*

The analyses of Dobson (1971), Elliott (1972*b*) and §6 extend to higher frequencies than the analyses of Snyder (1974) and §7, which are limited by an inability to estimate reliable directional spectra at higher frequencies. Thus the differences in results may be evidence that some other frequency-related parameter whose 'typical' value differs between the two analyses is important to the dynamics.

(*c*) *Polynomial fit characteristics*

The reliability of polynomial fits typically deteriorates near end points. Furthermore the data base for the fits of §7 is sparse for μ greater than about 2·5. As a result the extreme negative excursion of the §7 Re γ (for $\mu \sim 3$) is somewhat unreliable. Because of the complexity of the fitting procedures employed, a quantitative analysis of the the reliability of the §7 analysis has not been attempted. Note that the analysis of Snyder (1974) does not involve a polynomial fit and therefore is essentially no less reliable for $\mu \sim 3$ than elsewhere.

(*d*) *Instrumental differences*

The data bases for the various analyses under discussion differ with respect to instrumentation. In particular the §6 analysis involves only BIO instruments, while the §7 analysis involves both BIO and Nova instruments (there were seven pressure sensors, three from BIO, and six wave sensors, two from BIO). Although the calibration of all instruments was carefully checked in the laboratory prior to the field experiment, and regular intercomparisons in the field were made, it is conceivable that

field conditions might induce systematic differences between these instruments. Note, however, that comparison of the best fit cross spectral estimates of §7 with the observed estimates (both BIO and Nova instrument pairs) does not suggest any obvious systematic differences.

(e) *Differences in Fourier analysis techniques*

The spectral analysis algorithms used at BIO and Nova have been compared and found to give essentially the same results. Differences are well within the 95% confidence limits associated with the analyses.

In summary our best guess after correction for μ scaling is that for conditions similar to those which occurred at the Bight of Abaco site in winds of 5 to 10 m s^{-1}, the 'mean' γ lies somewhere between the estimates of §§6 and 7. In the range $1 < \mu < 3$ the imaginary part of γ is given approximately by

$$\operatorname{Im}\gamma \sim (0{\cdot}2 \text{ to } 0{\cdot}3)(\mu - 1).$$

For $\mu < 3$ the dependence of $\operatorname{Re}\gamma$ on μ is roughly parabolic with a maximum ($\simeq 0$) somewhere in the range $\mu = 1{\cdot}2$ to $1{\cdot}5$. For $\mu = 3$, $\operatorname{Re}\gamma \sim -1$ to -2. $\operatorname{Arg}\gamma$ falls rapidly to a minimum of $\sim 120°$ to $135°$ at $\mu = 1{\cdot}2$ to $1{\cdot}5$, then rises slowly with increasing μ. The details of these dependences vary with data set and/or mode of analysis. In each case the scatter about the mean is large.

The differential energy and momentum transfer to the (ω, θ) wave component are given by $\rho g A_{\zeta^2}$ and $\rho g(\mathbf{k}/\omega) A_{\zeta^2}$, respectively. Neglecting the turbulent contribution, the corresponding integral momentum transfer (or wave-supported stress) τ_{in} is

$$\tau_{\text{in}} = s\rho g \int_0^\infty d\omega \int_{-\pi}^{\pi} d\theta \mathbf{k}(\omega, \theta) \operatorname{Im}\gamma[\mu(\omega, \theta), 0] E_{\zeta^2}(\omega, \theta). \tag{19}$$

The unidirectional model of §6 gives a downwave stress

$$\tau_{\text{in}} = \frac{1}{g} \int_0^\infty d\omega \omega^2 \operatorname{Im} G_{\zeta P}(0, 0, \omega).$$

The ratio between this stress and the total wind stress is

$$\tau_{\text{in}}/\tau = \int_0^\infty d\tilde{\omega} H_{\text{in}}(\tilde{\omega}),$$

where $\tilde{\omega} = \omega/\omega_m$ is dimensionless frequency (ω_m is peak frequency), and

$$H_{\text{in}}(\tilde{\omega}) = \frac{\tilde{\omega}^2 \omega_m^3}{g\tau} \operatorname{Im} G_{\zeta P}(0, 0, \tilde{\omega}\omega_m).$$

With $\cos^2\theta$ spreading the simplified model of §6 gives a similar result with

$$H_{\text{in}}(\tilde{\omega}) = \frac{8}{3\pi} \frac{\tilde{\omega}^2 \omega_m^3}{g\tau} \operatorname{Im} G_{\zeta P}(0, 0, \tilde{\omega}\omega_m).$$

Correcting for the horizontal displacement of the sensors and extrapolating to the surface (with $\chi = 0{\cdot}86$), estimates of (19) were computed for runs 15 to 20 (figure 24) and the wave follower runs (figure 25).

Clearly the present data do not extend to sufficiently high frequency to properly

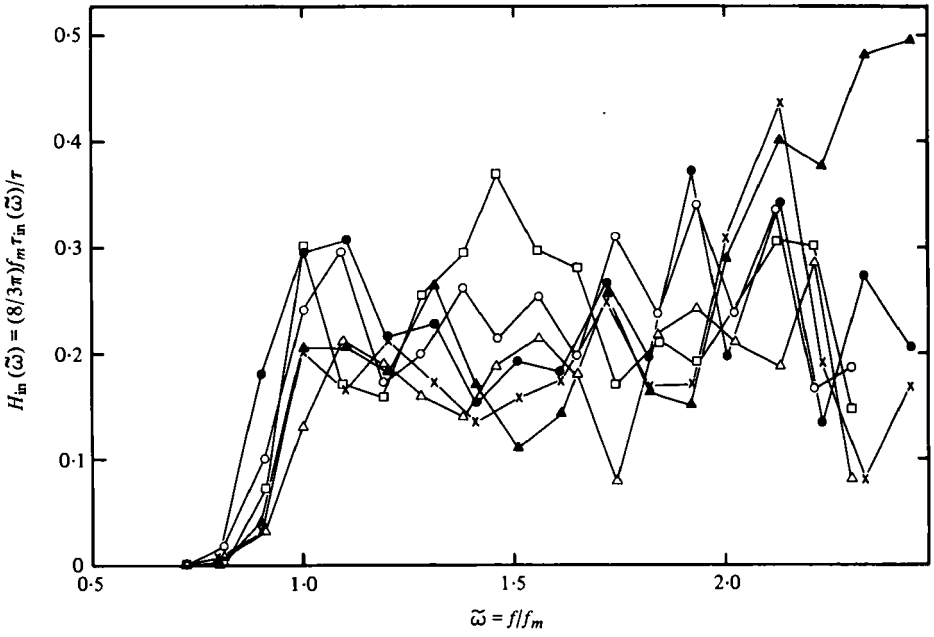

FIGURE 24. $f_m H(\tilde{\omega}) = (8/3\pi) f_m \tau_{in}(\tilde{\omega})/\tau$ versus $\tilde{\omega} = f/f_m$, for the following runs: △, 15; □, 16; ○, 17; ×, 18; ▲, 19; ●, 20.

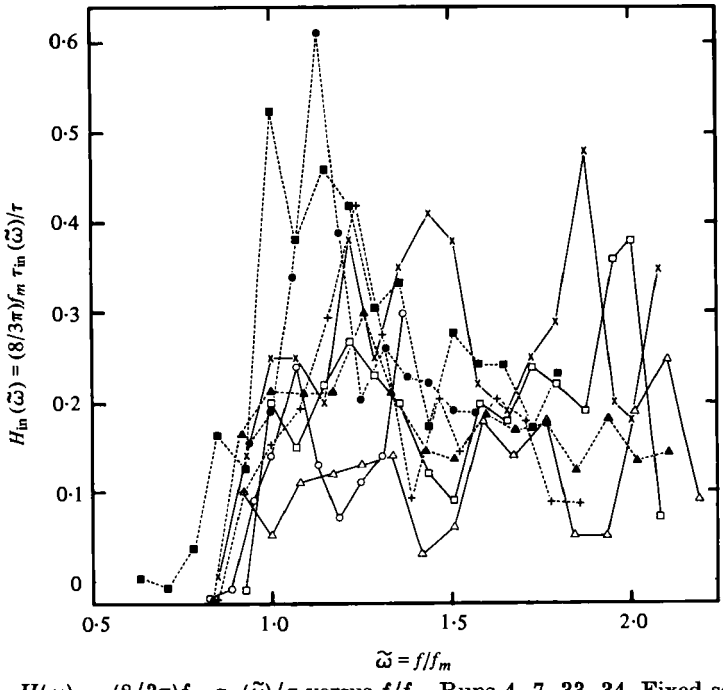

FIGURE 25. $f_m\ H(\omega) = (8/3\pi) f_m\ \tau_{in}(\tilde{\omega})/\tau$ versus f/f_m. Runs 4, 7, 33, 34. Fixed sensors: ×, ○, △, □. Wave follower: +, ●, ▲, ■.

Run	f_m(Hz)	τ_{in}/τ
4	0·54	0·70
5	0·54	0·56
6	0·54	0·60
7	0·65	0·20
15	0·42	0·64
16	0·42	0·77
17	0·42	0·77
18	0·38	0·72
19	0·38	0·81
20	0·38	0·91
21	0·38	0·32
22	0·38	0·35
25	0·42	0·61
33	0·46	0·44
34	0·54	0·47
4WF	0·54	0·49
7WF	0·65	0·46
33WF	0·46	0·51
34WF	0·54	0·58
		Mean 0·57

TABLE 9. Momentum transfer to waves as fraction of sonic stress for the run.

$$\tau_{in}/\tau = \int_0^\infty d\tilde{\omega}\, H_{in}(\tilde{\omega});$$ see equation (19) in text.

close the integral. Assuming that $G_{\zeta P}$ goes as ω^{-4} at high frequency [consistent with (18)] allows a rough estimate of total momentum transfer for these runs. As can be seen from table 9, this transfer is typically a large fraction of the measured wind stress determined from the sonic anemometer.

An estimate of the total momentum transfer in terms of the dimensionless fetch can be computed from (19) by using the JONSWAP spectral form for E_{ζ^2} (with $\cos^2\theta$ spreading) and relation (18) for $\mathrm{Im}\,\gamma(\mu, 0)$. A similar computation was presented by Snyder (1974) for several different $\mathrm{Im}\,\gamma(\mu, 0)$. Using Snyder's power laws for the JONSWAP parameters and casting the computation in terms of an effective drag coefficient C_{in} gives

$$C_{in}(\tilde{x}) = \int_0^\infty d\tilde{\omega} I_{in}(\tilde{\omega}, \tilde{x}), \tag{20}$$

where $\tilde{\omega}$ is dimensionless frequency and $\tilde{x}$ is dimensionless fetch. The integrand I_{in} is shown in figure 26 for various $\tilde{x}$. Consistent with the computations for the simplified model, the integrand is generally significant above $\tilde{\omega} > 3$. However, the importance of higher frequencies is a strong function of dimensionless fetch. Table 10 shows the ratio

$$R_{in}(\tilde{\sigma}, \tilde{x}) \equiv \frac{1}{C_{in}(\tilde{x})} \int_0^{\tilde{\sigma}} d\tilde{\omega}\, I_{in}(\tilde{\omega}, \tilde{x})$$

as a function of $\tilde{\sigma}$ for various $\tilde{x}$. These displays indicate that only at small dimensionless fetch is the momentum transfer determined by the spectral peak ($\tilde{\omega} < 3$). For large dimensionless fetch, it is the frequencies well beyond the spectral peak which are important.

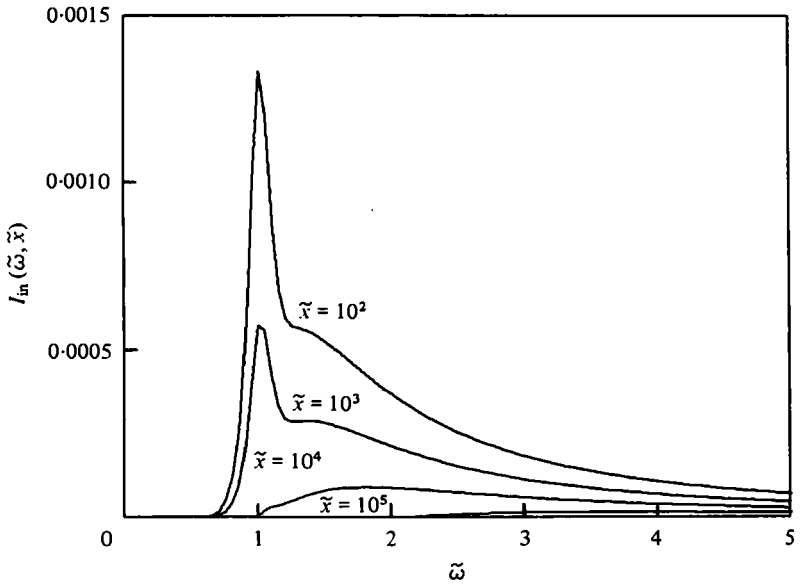

FIGURE 26. Integrand of (20) $I_{in}(\tilde{\omega}, \tilde{x})$. Based on the extrapolation $\text{Im}\,\gamma \equiv 0{\cdot}2(\mu - 1)$, $\mu \geqslant 1$, $\text{Im}\,\gamma \equiv 0, \mu < 1$.

	$R_{in}(\tilde{\sigma}, \tilde{x})$			
$\tilde{\sigma}$	$\tilde{x} = 10^2$	$\tilde{x} = 10^3$	$\tilde{x} = 10^4$	$\tilde{x} = 10^5$
1	0·09	0·06	0·00	0·00
2	0·46	0·39	0·18	0·00
3	0·63	0·57	0·39	0·06
4	0·72	0·67	0·53	0·19
5	0·77	0·73	0·61	0·30
7	0·84	0·81	0·73	0·46
10	0·88	0·86	0·81	0·61

TABLE 10. Closure of C_{in} integral. $\text{Im}\,\gamma = 0{\cdot}2\,(\mu - 1)$ extrapolation.

Figure 27 shows the resulting dependence of C_{in} on dimensionless fetch. Also shown are the drag coefficients C_{ad}, C_{hf}, C_{ds}, and the linear combinations $C_{ad} + C_{hf}$ and $C_{hf} + C_{ds}$ defined by Snyder (1974) from Hasselmann *et al.* (1973). The figure is analogous to the upper right-hand panel of Snyder's figure 19 [based on Elliott's 1972*b* results], which differs only in the choice of $\text{Im}\,\gamma$ for $\mu < 1$ (noticeable primarily at large dimensionless fetch, where the original choice predicts negative integral transfer). Consistent with the stress computations for the simplified model, and with the somewhat speculative conclusions of the JONSWAP experiment with respect to atmospheric input (which depend upon several assumptions for the dissipation), figure 27 suggests that the integral momentum transfer is a significant fraction of the wind stress. This fraction is an inverse function of dimensionless fetch ranging from ~ 1 for $\tilde{x} = 10^2$ (assuming a wind stress drag coefficient of $\sim 0{\cdot}002$) to $\sim 0{\cdot}1$ for $\tilde{x} = 10^5$.

We note that this computation depends heavily on the extrapolation of the linear

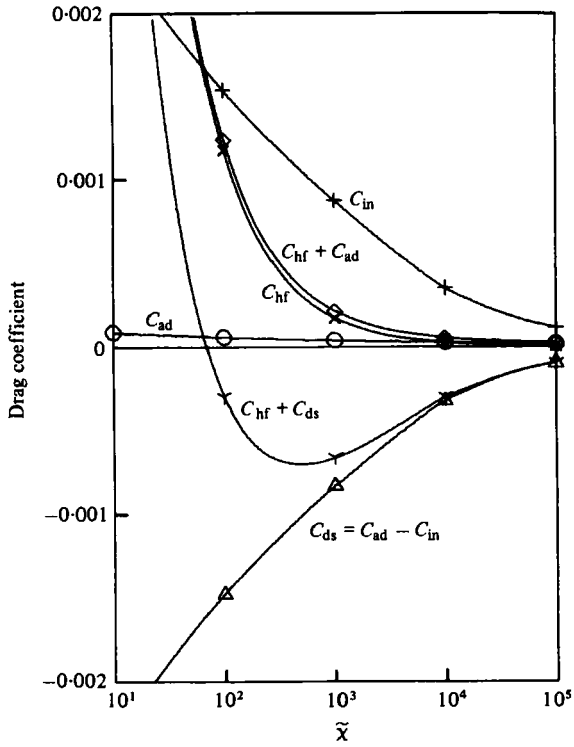

FIGURE 27. Fetch dependence of various drag coefficients. C_{in} is the coefficient of wave-supported drag. C_{ad} represents the momentum advected away by the wave field, C_{hf} the momentum transferred to high frequencies by nonlinear transfer, and C_{ds} the momentum dissipated. The estimate for C_{in} is based on the extrapolation $\text{Im}\,\gamma \equiv 0{\cdot}2(\mu - 1)$, $\mu \geqslant 1$, $\text{Im}\,\gamma \equiv 0$, $\mu < 1$.

dependence of $\text{Im}\,\gamma$ on μ above $\mu = 3$. In fact there is some indication in figure 22 that this dependence may be somewhat stronger than linear, which could increase the transfer substantially. However, we also note that figures 24–27 and tables 9 and 10 all assume zero drift current. Inclusion of drift would significantly reduce this transfer, via the factor **k** in (19).

10. Summary and conclusions

We have conducted a joint study of microscale fluctuations of atmospheric pressure above surface gravity waves. The primary objectives of the study were to resolve differences in previous independent field measurements and to estimate the vertical profile of wave-induced air pressure and the corresponding energy and momentum transfer to waves. A secondary objective was to build a quantitative description of the turbulent component of the air pressure.

The study began with an intercomparison of air pressure sensor instrumentation and calibration techniques. This intercomparison showed the following.

(1) Previous instrument calibrations by Snyder *et al.* (1974), assuming 'instantaneous' response for their pressure standard, were systematically biased at higher frequencies. Correction for this bias increases Snyder's (1974) estimates of energy and momentum transfer by about a factor of two.

(2) The reliability of present calibrations of the Nova and BIO fixed air pressure sensors is approximately $\pm 3\%$ in amplitude and $\pm 2°$ in phase, below 1 Hz.

(3) The wave follower-mounted air pressure sensor was somewhat temperature sensitive, exhibiting typical drifts of $\pm 5\%$ in gain.

Later analysis also shows that:

(4) the wave follower-mounted air-pressure sensor was also sensitive to vertical accelerations. A correction based on a post-experiment calibration of this sensitivity gives results which are reasonably consistent with fixed sensor measurements. The reliability of the wave follower pressure measurements is estimated to be roughly $\pm 5\%$ in amplitude and $\pm 10°$ in phase.

The intercalibration of instruments was followed by a month-long field experiment at Nova University's experimental site in the Bight of Abaco, Bahamas. A total of 37 data runs of varying duration and sensor mix were taken over a two-week period.

The data collected by BIO were analysed using techniques previously applied by Dobson and Elliott, modified to account for directional spreading. The entire data set was analysed by Snyder at Nova using a model fitting scheme which incorporates full directionality, mean current profile, vertical profile of wave-induced air pressure, and a model of the turbulent pressure field. The principal output of both data analyses is estimates for the complex dimensionless ratio γ between wave-induced air pressure and surface elevation in the ω plane, taken to be a function of dimensionless wind speed μ and dimensionless height λ (see §5).

Comparison of these analyses with the earlier results of Dobson (1971), Elliott (1972*b*) and Snyder (1974) suggest the following for conditions similar to those which apply in the Bight of Abaco with winds of 5 to 10 m s^{-1}.

(5) In the range $1 < \mu < 3$ and $1 < \lambda < 3$ the vertical dependence of the wave-induced air pressure is approximately exponential and slightly less steep than the potential theory result

$$|\gamma| = e^{-\lambda}.$$

The phase of γ is independent of λ. These conclusions are consistent with the previous findings of Elliott (1972*b*) and Snyder (1974), and with the predictions of Miles' (1957) theory. The Nova analysis yields a somewhat larger effective vertical decay (closer to potential theory) than does Elliott's analysis or the BIO analysis of the present data. This difference is probably the result of mean currents, included only in the Nova analysis.

(6) For $1 < \mu < 3$ the imaginary part of $\gamma(\mu, 0)$ is approximated by a relation of the form

$$\mathrm{Im}\,\gamma(\mu, 0) = (0{\cdot}2 \text{ to } 0{\cdot}3)(\mu - 1).$$

This relation is reasonably consistent with the earlier results of both Elliott and Snyder (after correcting for the response of his pressure standard) and with both analyses of the present data. Snyder and the Nova analysis favour a coefficient of 0·2; Elliott and the BIO analysis a coefficient of 0·3 (if allowance is made for directional spreading and drift). Dobson's (1971) results do not fit the pattern. Correction for drift (which was typically against the wind during his experiments) lowers his estimates of Im γ somewhat, but they are still several times larger than the others. We do not know if this difference reflects a difference in Dobson's experimental conditions, or some problem with his instrumentation and/or analysis. Because present wave follower results are

comparable with fixed sensor results, we do not believe that this difference suggests a radical depature from the exponential profile close to the water surface.

(7) For $\mu < 3$ the dependence of $\mathrm{Re}\,\gamma$ on μ is roughly parabolic with a maximum ($\lesssim 0$) somewhere in the range $\mu = 1{\cdot}2$ to $1{\cdot}5$. For $\mu = 3$, $\mathrm{Re}\,\gamma \sim -1{\cdot}0$ to $-2{\cdot}0$. $\mathrm{Arg}\,\gamma$ falls rapidly from $\sim 180°$ at $\mu = 1$ to a minimum of 120° to 135° at $\mu = 1{\cdot}2$ to $1{\cdot}5$, then returns more slowly towards 180° with increasing μ. The details of these dependences differ significantly depending on data set and/or mode of analysis. At large μ Snyder (1974) and the analysis of §7 typically find significantly larger $\mathrm{Re}\,\gamma$ and smaller $|(\mathrm{Arg}\,\gamma) - \pi|$ than do Elliott (1972*b*) and the analysis of §6. This discrepancy is felt to be partially but not entirely the result of inability to allow for directional spreading and drift in the analysis of §6, both of which affect the scale of μ.

(8) For $3 < \mu < 5$ it appears that $\mathrm{Im}\,\gamma$ continues to increase more or less linearly with μ, although there is some indication that the increase may be faster than linear.

(9) Analysis of limited backscatter observations does not support earlier conclusions by Dobson (1971) and Snyder (1974) that for $\mu < 0$ the wave field is strongly damped. This analysis suggests that the phase of the wave-induced pressure is essentially 180°.

(10) These findings are comparable with the predictions of Miles (1957). A precise comparison is difficult because of the choice of parametrization for γ. However inter-run differences do not appear to correlate with estimates of Miles' profile parameter Ω.

(11) The total wave-supported stress for the pressure experiments depends heavily on contributions from frequencies higher than those monitored. By extrapolating present results beyond $\mu = 3$ we estimate that this stress is a significant fraction of the total wind stress (average of 0·4 to 0·7, depending on analysis). This same extrapolation suggests that for a JONSWAP spectrum this fraction varies between 1, for a dimensionless fetch $\tilde{x} = 10^2$, and 0·1, for $\tilde{x} = 10^5$.

The difficulty in reconciling various observations and analyses of the wave-induced pressure field and the large scatter within the individual analyses suggest the following.

(12) The parametrization of γ in terms of μ and λ, while useful, is probably inadequate. At least one other parameter is probably important to the dynamics.

(13) In designing experiments to measure wave-induced pressure and in interpreting the resulting data, it is important to account for (*a*) the vertical structure of the pressure field, (*b*) the directional properties of the wave spectrum, and (*c*) mean current. In the present case we have dealt with these considerations by employing a three-dimensional array of wave and air-pressure sensors and by determining drift as part of the directional spectrum analysis. Direct measurement of the mean current profile would have been preferable.

Analysis of the turbulent component of the air-pressure field and comparison with earlier measurements by Priestley (1965) and Elliott (1972*c*) suggest that:

(14) for the higher wind speed runs, the downwind coherence scale of the turbulent component of the air-pressure field is typically larger by an order of magnitude than the crosswind coherence scale, consistent with a 'frozen' turbulence hypothesis.

We therefore speculate two things:

(15) The loss of coherence observed by Priestley (1965) and by Elliott (1972*c*) along the wind axis does not reflect the true downwind coherence scale but results from variations in mean wind direction. We conclude that the turbulent contribution to wave growth is larger or smaller than that implied by Priestley's results, depending on how close to resonance a particular component is.

(16) An appropriate statistical description of the turbulent pressure field is contained in the 'intrinsic' turbulent pressure spectrum $F_{Q^2}(\mathbf{k})$. This spectrum is typically reasonably isotropic and decays as $k^{-\nu}$ where $\nu = -2$ to -3. Estimates for this spectrum are computed for the present data from the cross-spectra between air-pressure sensors.

The present effort by no means exhausts the possibilities for further experimental investigations of air pressure fluctuations over waves. We have by design concentrated our attentions on fluctuations induced by wave components in the range of dimensionless wind speed $1 < \mu < 3$. We suggest that the following ranges are of sufficient interest to warrant further study.

(*a*) $3 < \mu$. This range is crucial to an accurate estimate of the total wave-supported stress. Measurements could be obtained from instrumentation similar to that employed in the present experiments (the response of the Nova air-pressure sensors would have to be improved) provided the site of the measurements was at small dimensionless fetch. Wave-follower measurements would be particularly useful. The problem with fixed sensor measurements at larger dimensionless fetch is that such sensors cannot be placed close enouth to the mean water surface to monitor properly the frequencies of interest.

(*b*) $0 < \mu < 1$. This range is important to understanding the energy balance at large dimensionless fetch, where damping for small μ could provide an effective brake for the evolution of the wave spectrum. Here the appropriate measurement should be made at large dimensionless fetch, either at an open bank site using instrumentation similar to that employed in the present experiments or on the open sea using free-floating, pressure-sensing, pitch/roll buoys.

(*c*) $\mu < 0$. This range is important to understanding what happens to the sea with a contrary wind. Here fixed sensor measurements in the vicinity of a vertical breakwater should provide an appropriate means for evaluating γ.

The authors are indebted to the Government of the Bahamas for allowing us to perform our experiment in the Bight of Abaco, and to the University of Miami for the use of R/V *Calanus*. Erik Banke kept the BIO party organized and produced the sonic anemometer results; David Hunley and David Harvey kept the instruments running for Nova and BIO respectively. The expedition cook, Barbara Long, maintained a high culinary standard throughout. Linda Smith carried out much of the Nova data analysis and prepared many of the figures. The Nova group was supported by NSF Grant DES74-19843; travel funds for the BIO group and for three data-analysis workshops were provided by the NATO Air/Sea Interaction Special Program Panel under Grants SV-6, 7 and 9.

REFERENCES

Barnett, T. P. & Wilkerson, J. C. 1967 On the generation of wind waves as inferred from air-borne radar measurements of fetch-limited spectra. *J. Mar. Res.* **25**, 292–328.

Bingham, C., Godfrey, M. D. & Tukey, J. W. 1967 Modern techniques of power spectrum estimation. *I.E.E.E. Trans. Audio and Electroacoustics* AU-15.

Dobson, F. W. 1971 Measurements of atmospheric pressure on wind-generated sea waves. *J. Fluid Mech.* **48**, 91–127.

DOBSON, F. W. & ELLIOTT, J. A. 1978 Wave-pressure correlation measurements over growing sea waves with a wave follower and fixed-height pressure sensors. *Turbulent Fluxes through the Sea Surface, Wave Dynamics and Prediction* (ed. A. Favre & K. Hasselmann). Plenum.

ELLIOTT, J. A. 1972*a* Instrumentation for measuring static pressure fluctuations within the atmospheric boundary layer. *Boundary-Layer Met.* **2**, 476–495.

ELLIOTT, J. A. 1972*b* Microscale pressure fluctuations near waves being generated by the wind. *J. Fluid Mech.* **54**, 427–448.

ELLIOTT, J. A. 1972*c* Microscale pressure fluctuations measured within the lower atmospheric boundary layer. *J. Fluid Mech.* **53**, 351-383.

HARVEY, D. R. & DOBSON, F. W. 1976 The Bedford Institute Wave Follower. *Bedford Inst. of Oceanog. Dartmouth, N.S., Canada. Int. Rep.* BI-R-76-13.

HASSELMANN, K. 1960 Grundleichungen der Seegangsvoraussage. *Schiffstechnik* **7**, 191–195.

HASSELMANN, K. 1962 On the non-linear energy transfer in a gravity-wave spectrum. 1. General theory. *J. Fluid Mech.* **12**, 481–500.

HASSELMANN, K. 1974 On the spectral dissipation of ocean waves due to whitecapping. *Boundary-Layer Met.* **6**, 107–127.

HASSELMANN, K., BARNETT, T. P., BOUWS, E., CARLSON, H., CARTWRIGHT, D. E., ENKE, K., EWING, J. A., GIENAPP, H., HASSELMANN, D. E., KRUSEMANN, P., MEERBURG, A., MÜLLER, P., OLBERS, D. J., RICHTER, K., SELL W. & WALDEN, H. 1973 Measurements of wind-wave growth and swell decay during the Joint North Sea Wave Project (JONSWAP). *D.H.I. Zeitschrift* A(8), 12.

LONG, R. B. 1980 A parametrical model for the vertical structure of the induced atmospheric pressure field above a spectrum of surface gravity waves. *J. Fluid Mech.* **99**, 163–183.

LONGUET-HIGGINS, M. S., CARTWRIGHT, D. E. & SMITH, N. D. 1963 Observations of the directional spectrum of sea waves using the motions of a floating buoy. In *Ocean Wave Spectra*, pp. 111–132. *Proc. Conf. on Ocean Wave Spectra, Easton, Md, U.S.A.*, 1961. Prentice-Hall.

MILES, J. W. 1957 On the generation of surface waves by shear flows. *J. Fluid Mech.* **3**, 185–204.

MILES, J. W. 1959 On the generation of surface waves by shear flows. Part 2. *J. Fluid Mech.* **6**, 568–582.

MITSUTA, Y. 1968 Application of sonic anemometer-thermometer to the studies of vertical eddy transport processes in the atmospheric boundary layer. *Spec. Contrib., Kyoto Univ.* **8**, 45–60.

PEEP, M. & FLOWER, R. J. 1969 The Chesapeake Bay Institute Wave Follower. *The Johns Hopkins University, Chesapeake Bay Inst., Baltimore, Md, Tech. Rep.* 73.

PHILLIPS, O. M. 1957 On the generation of waves by turbulent wind. *J. Fluid Mech.* **2**, 417–445.

PRIESTLEY, J. T. 1965 Correlation studies of pressure fluctuations on the ground beneath a turbulent boundary layer. *U.S. Nat. Bureau Standards Rep.* 8942.

ROSS, D. B. & CARDONE, V. J. 1978 A comparison of parametric and spectral hurricane wave prediction products. *Turbulent Fluxes through the Sea Surface, Wave Dynamics and Prediction* (ed. A. Favre K. Hasselmann). Plenum.

SHEMDIN, O. H. & HSU, E. Y. 1967 Direct measurement of aerodynamic pressure above a simple progressive gravity wave. *J. Fluid Mech.* **30**, 403–416.

SNYDER, R. L. 1974 A field study of wave-induced pressure fluctuations above surface gravity waves. *J. Mar. Res.* **32**, 497–531.

SNYDER, R. L. & COX, C. S. 1966 A field study of the wind generation of ocean waves. *J. Mar. Res.* **24**, 141–178.

SNYDER, R. L., LONG, R. B., IRISH, J., HUNLEY, D. G. & PFLAUM, N. C. 1974 An instrument to measure atmospheric pressure fluctuations above surface gravity waves. *J. Mar. Res.* **32**, 485–496.

WIENER, N. 1949 *Extrapolation, Interpolation, and Smoothing of Stationary Time Series.* Massachusetts Institute of Technology Press.

WILLMARTH, W. W. & WOOLDRIDGE, C. E. 1962 Measurements of the fluctuating pressure at the wall beneath a thick turbulent boundary layer. *J. Fluid Mech.* **14**, 187–210.